

Interpretable statistical representations of neural population dynamics and geometry

Adam Gosztolai,^{1*} Robert L. Peach,² Alexis Arnaudon,^{3,4}
Mauricio Barahona,⁴ Pierre Vanderghyest¹

¹Signal Processing Laboratory (LTS2), EPFL, Lausanne, 1016, Switzerland

²Department of Neurology, University Hospital Würzburg, Würzburg, 97070, Germany

³Blue Brain Project, EPFL, Campus Biotech, 1202, Geneva, Switzerland

⁴Department of Mathematics, Imperial College London, London, SW7 2AZ, United Kingdom

*To whom correspondence should be addressed; E-mail: adam.gosztolai@epfl.ch.

Abstract

The dynamics of neuron populations during many behavioural tasks evolve on low-dimensional manifolds. However, it remains challenging to discover latent representations from neural recordings that are interpretable and consistently decodable across individuals and conditions without explicitly relying on behavioural information. Here, we introduce MARBLE, a fully unsupervised geometric deep learning framework for the data-driven representation of non-linear dynamics based on statistical distributions of local dynamical features. Using both *in silico* examples from non-linear dynamical systems and recurrent neural networks and *in vivo* recordings from primates and rodents, we demonstrate that MARBLE can infer latent representations that are highly interpretable in terms of global system variables such as decision-thresholds, kinematics or internal states. We also show that MARBLE representations are consistent across neural networks and animals, so that they can be used to compare cognitive computations or train universal decoders. Through extensive benchmarking, we show that unsupervised MARBLE provides best-in-class within- and across-animal decoding accuracy, comparable to or significantly better than current supervised approaches, yet without the need for behavioral labels. Our results suggest that using the manifold structure in conjunction with temporal information of neural dynamics provides a common framework to develop better decoding algorithms and assimilate data across experiments.

Introduction

It is increasingly recognised that computations in the brain and in artificial neural networks can be understood as outputs of a high-dimensional dynamical system conformed by the activity of large populations of neurons¹⁻³. A prominent line of research has observed that behaviourally-relevant neural activity often takes place on low-dimensional smooth subspaces of the full state space, usually called *neural manifolds*⁴⁻¹². From this perspective, several works have focused on how the geometry^{4,7,13,14} or topology^{6,8,9} of neural manifolds relates to the underlying task or computation. By contrast, others have suggested that dynamical flows of neural population activity have an equally prominent role^{11,15-17} and that the geometry of the manifold is merely an imprint that changes over time or across individuals⁴. Although recent experimental techniques provide means to simultaneously record the activity of large neuron populations¹⁸⁻²⁰, revealing the structure of the underpinning latent dynamical processes from data and interpreting their relevance in computational tasks remains a fundamental challenge¹⁶.

Overcoming this challenge requires computational frameworks that leverage the manifold structure of neural dynamical flows for the unsupervised discovery of its behavioural correlates. Yet current

techniques fall short of this aim. Indeed, unsupervised dimensionality reduction approaches, both linear methods such as PCA or non-linear manifold learning methods such as t-SNE²¹ or UMAP²², treat the neural activations as a point cloud, from which they infer a manifold but cannot distinguish different dynamical processes that distributionally yield the same manifold. Alternatively, dynamical systems models can be used to learn temporal information of neural activity^{23–28}. However, these models depend on the particular embedding of trajectories in state space and, in turn, the measured variables (i.e., neurons), hindering their ability to compare representations across experiments. Topological data analysis methods can circumvent some of these issues by characterising invariant structures in the data, e.g., loops⁶ and tori⁹. However, these methods are designed to capture qualitative behaviours and changes (e.g., bifurcations) but fail to capture quantitative changes in dynamics and geometry that can be crucial during representational drift⁴ or gain modulation²⁹. Only recently, representation learning methods such as pi-VAE [30] and CEBRA [31] have been introduced to infer interpretable latent embeddings of neural trajectories and provide accurate decoding thereof into behaviour. Yet, these methods are either supervised or self-supervised, i.e., requiring user-defined ground-truth labels such as task conditions, kinematics, or time labels. This is undesirable during discovery as such labels are often unavailable or can introduce unintended correspondence between experimental conditions or trials. For the same reasons, supervised approaches cannot provide an unbiased distance metric to compare neural dynamics across conditions or systems.

Here, we introduce a fully unsupervised representation-learning method called MARBLE, or MAnifold Representation Basis LEarning, which obtains highly interpretable and decodable representations from neural dynamics and provides a well-defined similarity metric between dynamical processes, even in different systems. MARBLE combines ideas from empirical dynamical modelling³² and the statistical descriptions of collective systems^{33,34} to represent non-linear dynamics over manifolds. Specifically, stemming from notions in differential geometry, MARBLE decomposes the dynamics into a set of local flow fields around each sample point and uses them to encode global information of the dynamics by building a similarity-preserving embedding using geometric deep learning^{35–37} and unsupervised contrastive learning³⁸. We show that MARBLE representations inferred from electrophysiological recordings of the premotor cortex of macaques during a reaching task and of the hippocampus of rats during a spatial navigation task are substantially more interpretable and decodable than those obtained using current representation learning frameworks [31]. Further, the local viewpoint of MARBLE provides a robust similarity metric between the sparsely and irregularly sampled dynamical systems typical in neural recordings obtained over a limited number of trials. We show that this data-driven metric is expressive enough to infer continuous and qualitative changes in the dynamical landscape of recurrent neural networks during sensory gain modulation or in decision-making tasks at the decision threshold, respectively. Finally, we show that MARBLE facilitates comparing dynamics across entirely different systems by discovering consistent embeddings across animals without auxiliary transformations and offering a well-defined similarity metric irrespective of the embedding of the dynamics.

Our results suggest that differential geometric notions can reveal as yet unaccounted-for non-linear variations in neural data that can further our understanding of neural dynamics underpinning neural computations and behaviour.

Results

Unsupervised data-driven distributional representation of vector fields over manifolds

To characterise neural computations during a task, e.g., decision-making or arm-reaching, a typical experiment involves a set of trials under condition c , e.g., a given stimulus or task condition, producing a corresponding set of d -dimensional time-series $\{\mathbf{x}(t)\}$ of neural activity, e.g., firing rate or fluorescence intensity. Here, d is the number of neurons or a dimensionally-reduced set of variables. Frequently, one performs recordings under diverse conditions and seeks to discover, without supervision, how the structure of neural dynamics relates to task structure. In other setups, one may desire to compare trajectories across conditions or even animals to reveal alterations in neural mechanisms. Both applications are challenging as trajectories initialised differently across trials produce uneven and possibly sparse sampling of the relevant state space features so that similar dynamics may unfold

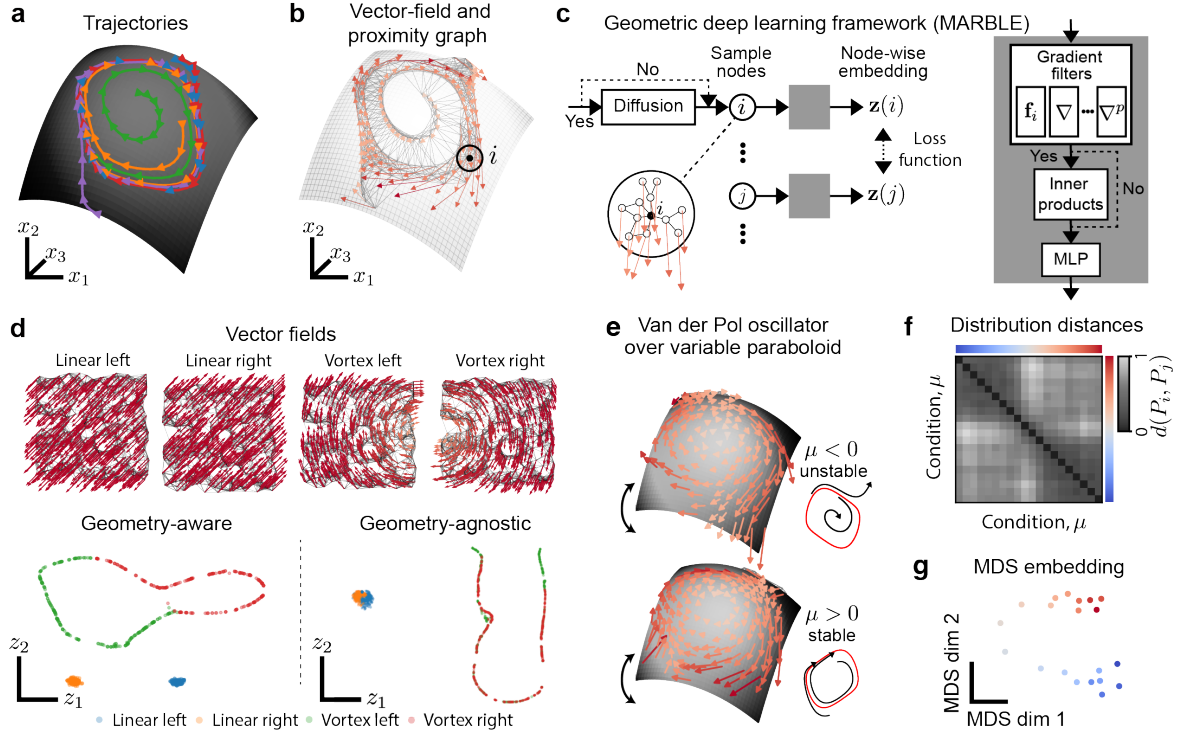


Figure 1: **Data-driven statistical representation of measured dynamics over manifolds.** **a** Trajectories measured in different trials (colours) evolving over a latent manifold. **b** Vector field representation of trajectories. A k -nearest neighbour graph approximates the manifold. The black circle marks a sample point and its corresponding local flow field (LFF). **c** Geometric deep learning model, MARBLE, for the node-wise embedding of LFFs. The vector field is smoothed by an optional vector diffusion layer. The LFFs are approximated to p -th order by gradient filters and optionally transformed into rotation-invariant inner product features. Finally, a multilayer perceptron (MLP) performs a node-wise similarity-preserving embedding of LFFs into a latent space. **d** Top: four toy vector fields, two constant and two rotational fields. Bottom: geometry-aware and geometry-agnostic MARBLE embeddings. Geometry-aware embeddings distinguish rotational information in LFFs, whereas geometry-agnostic embeddings learn only vector field expansion and contraction. **e** Vector fields of the Van der Pol oscillator over a paraboloid of variable curvature in the unstable ($\mu = -0.25$) and stable ($\mu = 0.25$) regimes sampled from randomly initialised trajectories. Insets show the limit cycle in red and representative trajectories from a vertical projected view. **f** Distribution distances across conditions. Clustering indicates an abrupt dynamical change at $\mu = 0$. **g** Two-dimensional MDS embedding of the distribution distance matrix recovers the ordering of parameter μ over two weakly connected one-dimensional manifolds.

over manifolds with different embeddings across subjects or conditions^{4,27}.

To address these challenges, MARBLE departs from the current modelling paradigm of learning the temporal evolution of the states in single isolated trajectories^{27,28,31}. Instead, it represents the dynamics statistically over ensembles of trajectories using a latent distribution obtained from the local dynamical context of each sample point. This is possible as the trajectories of neural dynamics¹⁵ or, more generally, of dissipative dynamical systems³⁹ converge to a submanifold of the original d -dimensional state space (Fig. 1a). We may equivalently treat the trajectories from a set of trials under a given experimental condition c as a vector field $\mathbf{F}_c = (\mathbf{f}_1, \dots, \mathbf{f}_n)$ anchored to a point cloud $\mathbf{X}_c = (\mathbf{x}_1, \dots, \mathbf{x}_n)$ (Fig. 1b), where n is the number of sample points, e.g., recorded neural activations across all trials under this condition. By approximating the underlying manifold using a proximity graph to \mathbf{X}_c , we define the dynamical context of a point i as the local flow field (LFF) supported on points that are at most a distance p from i measured over the graph. We jointly embed individual LFFs into a E -dimensional shared latent space to represent the dynamical system as an empirical distribution P_c formed by a collection of features $\{\mathbf{z}_i\}$. To define a metric between dynamical systems

under conditions c and c' , we use the optimal transport distance (Eq. S18), $d(P_c, P_{c'})$, between their distributional latent representations, which generally outperforms entropic measures (e.g., KL divergence) when detecting complex interactions based on overlapping distributions³⁴.

We note that the above approach is substantially different from classical dimensionality reduction approaches such as PCA, t-SNE or UMAP, which map the neural activity \mathbf{x}_i directly into latent features and, therefore, are oblivious to the dynamics that have generated the point cloud X_c . By learning the variation of the vector field within the LFF around each point, we also learn dynamical information, which substantially enhances the representational capability of our method.

Unsupervised learning of the latent representation P_c follows from the continuity of LFFs over the manifold, which means that close LFFs are more similar than randomly sampled ones. To capture global information using LFFs, we develop a similarity-preserving embedding of LFFs using a geometric deep learning architecture consisting of four components (Fig. 1c, see Sect. S1 in Materials and Methods). Following an optional vector diffusion kernel with learnable parameter τ (Eq. S3) which tunes the spatial extent of the LFFs we apply: (i) p gradient filter layers whose output together with \mathbf{f}_i gives the best p -th order approximation of the LFF around i (Figs. S1–S3, Eq. S13); (ii) inner product features involving learnable linear transformations which make the gradient features rotation invariant (Figs. S4–S5, Eq. S15); and (iii) a multilayer perceptron (MLP) with learnable weights ω that produces the latent feature \mathbf{z}_i .

We perform unsupervised training via a soft constraint in the loss function (Eq. S17) to learn to embed adjacent LFFs over the graph to lie close by whereas randomly sampled LFFs are placed further apart. In contrast to supervised representation-learning methods^{30,31}, MARBLE embeds LFFs across all manifolds (i.e., conditions) with shared weights, and thus assigns similar latent features to similar LFFs across conditions, allowing their unsupervised comparison.

Comparing dynamics within and across systems: geometry-aware *vs.* geometry-agnostic representations

The inner product features in MARBLE give rise to two operation modes that can be exploited to provide insights about the inferred neuronal representations. To illustrate this issue, we consider a toy model consisting of linear and constant (rotational) vector fields over a two-dimensional plane ($d = 2$, trivial manifold) in Fig. 1d, top. As shown later, MARBLE can capture complex non-linear dynamics over non-linear manifolds beyond this simple illustrative example. In geometry-aware mode, the inner product features are disabled (Fig. 1c), allowing MARBLE to learn the orientation of the LFFs, ensuring maximal expressivity and interpretability. In our toy example, constant fields (left and right) are mapped into two distinct clusters, whereas rotational fields are distributed based on their angular orientation (Fig. 1d, bottom). This mode of operation in MARBLE is useful when representing dynamics across conditions within a given animal or neural network, i.e. when the same neurons are sampled (Fig. 1d-g, Fig. 3-4b,c), or when the geometry of the neural manifold is essential to characterise the behaviour (Fig. 4e).

In geometry-agnostic mode, on the other hand, the inner product features are present and make the learnt features rotation invariant. In our toy example, this means that vector fields are no longer distinguishable based on LFF orientation, but we still capture other differences, e.g., expansion and contraction of the flows (Fig. 1d, bottom). This geometry-agnostic mode is able to discount the arbitrary rotations in the LFFs induced by different embeddings⁴⁰ (Figs. S4–S5), and is therefore useful when comparing across systems, such as neural networks trained from different initialisations (Fig. 2h-j). To demonstrate this for a non-linear dynamical system on a non-linear manifold, we analysed the Van der Pol oscillator mapped to a paraboloid while varying the damping parameter μ and the manifold curvature (Fig. 1e, see Sect. S3.1 in Materials and Methods). Using short simulated trajectories from random initial conditions for 20 different values of μ , we trained a geometry-agnostic MARBLE network to jointly embed the corresponding vector fields into a shared latent space ($E = 5$). Despite the sparse and irregular sampling, we detected robust dynamical variation as μ was varied. Specifically, the matrix of distribution distances $D_{cc'} = d(P_c, P_{c'})$ displays a two-partition structure, indicating the presence of two different types of dynamic behaviours (stable and unstable) separated by the Hopf bifurcation at $\mu = 0$ (Fig. 1f). This result is observed independently of manifold curvature (Fig. S6). Furthermore, and despite the irregular and sparse sampling across conditions, embedding $D_{cc'}$ using multidimensional scaling (MDS) revealed a one-dimensional manifold that captures the variation of μ and consequent compression and expansion of flow (Fig. 1g). Notably, this continuous

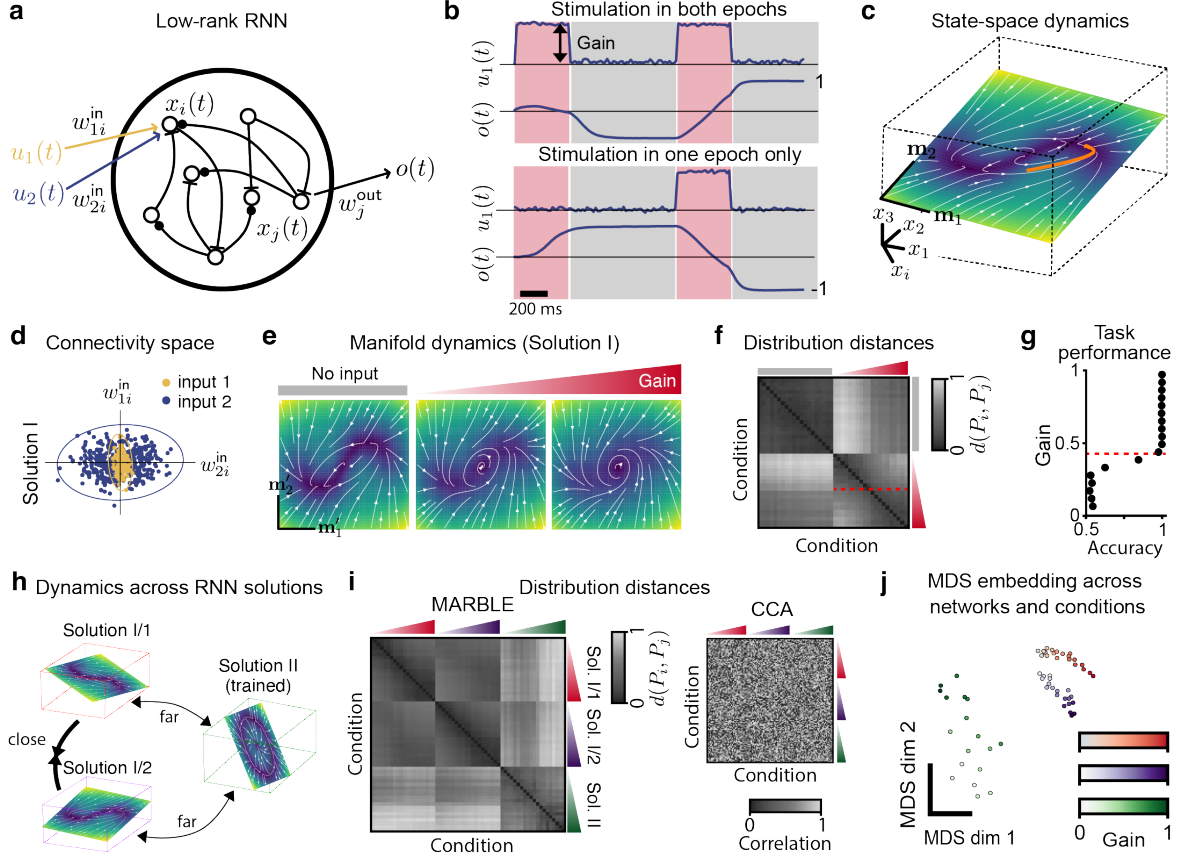


Figure 2: Statistical representations represent and discriminate computations across recurrent neural networks. **a** Low-rank RNN takes two stimuli as input and produces a decision variable as a read-out. **b** Representative stimulation patterns and decision outcomes for the delayed-match-to-sample task (one stimulus shown). Input amplitude equals the ‘gain’ during stimulation epochs (red) and zero otherwise (grey). **c** Neural dynamics of a trained rank-two RNN evolves on a randomly oriented plane in neural state space. Phase portrait shows mean field dynamics superimposed with a trajectory during a trial (orange). **d** Input weight space to neurons in a trained RNN. Colours are obtained by k-means clustering, indicating subpopulations specialised in respective inputs in **a**. Ellipses represent 3 std of fitted Gaussian distributions. **e** Phase portraits for different stimulus gains (0, 0.32, 1.0). **f** Distribution distances across gains obtained from geometry-aware embeddings. Hierarchical clustering indicates two clusters in the non-zero gain region, showing a qualitative change, i.e., bifurcation (red dashed line). **g** The inferred bifurcation point predicts the drop in task performance. **h** Networks trained from different initialisations can have different dynamics over differently embedded manifolds (Solution I, Solution II). As a control, we sampled networks from the weight distribution in **d** to obtain the same dynamics over differently embedded manifolds (Solution I/1, Solution I/2). **i** Distribution distances across the three networks and gains obtained from geometry-agnostic embeddings compared with that obtained from CCA. **j** MDS embedding of the distance matrix in **i** shows quantitative, continuous variation and alignment of gain-modulated conditions across similar dynamics.

manifold was not captured when training a geometry-aware network on the same data (Fig. S6), thus confirming that geometry-agnostic MARBLE can extract both abrupt and continuous dynamical variation while being invariant to manifold embedding at a slight loss of expressivity compared to the geometry-aware mode.

Discriminating computational mechanisms in recurrent neural networks

There has been significant recent interest in RNNs as surrogate models for the computations performed by the brain^{15,41–43}. Previous approaches for comparing RNN computations for a given task relied on representations of population activity as point clouds, which were then compared using shape analysis^{14,41,44}. However, these methods cannot distinguish dynamics producing similar point cloud distributions.

To demonstrate the advantages of MARBLE’s LFF-based representation, we trained RNNs with a rank-two connectivity matrix (Fig. 2a, see Sect. S3.2 in Materials and Methods) on the delayed-match-to-sample task⁴⁵. Rank-two RNNs were previously shown to be sufficiently expressive to learn this task⁴⁶. This common contextual decision-making task comprises two distinct stimuli with variable gain and two stimulation epochs of variable duration interspersed by a delay (Fig. 2b). Setting the gain to unity, the RNN was trained to converge to an output of 1 if either stimulus was presented during both epochs and -1 otherwise (Fig. 2b). As expected⁴⁷, the neural dynamics of a trained network during a trial evolves on a randomly oriented plane in state space (Fig. 2c and Fig. S7a-c). Yet we found that differently initialised networks produce two classes of solutions characterised by the clustering of their input weight distributions $\mathbf{w}_1^{\text{in}}, \mathbf{w}_2^{\text{in}}$ (Eq. S22): solution I consists of two subpopulations specialised in sensing the two stimuli (Fig. 2d), whilst in solution II the nodes generalise across the two stimuli (Fig. S7d). These two solutions exhibit substantially different neural dynamics consisting of multiple fixed points, saddles and line attractors, as shown by two representative examples, which we selected for further analysis (Fig. 2e, Fig. S7e).

We first asked whether MARBLE could infer dynamical neural correlates of loss of task performance as the stimulus gain is decreased. For 20 different input gains, we simulated 200 randomly initialised trials. For each gain, we extracted the part of the trajectories where the stimulus was present and used the remainder of the trajectory as a negative control because we expected no gain-related variation therein. We then trained a geometry-aware MARBLE network to embed all groups into a common latent space. The resulting matrix of pairwise distribution distances exhibits a block-diagonal structure (Fig. 2f). The top left block contains vanishing entries corresponding to the zero-gain controls, implying that MARBLE is robust to sampling variability. The other two subblocks of the bottom right block indicate a quantitative change in dynamics, which remarkably corresponds to a sudden drop in task performance (Fig. 2g) from 1 to 0.5 (random). This shows that MARBLE enables the unsupervised detection of dynamical events that are interpretable in terms of global decision variables.

Next, we asked if MARBLE can define a similarity metric for the dynamics across distinct RNNs. To this end, we took network Solutions I and II, which have different dynamics evolving over differently embedded manifolds (Fig. 2h). As a negative control, we randomly sampled two new networks from the weight distribution of Solution I because low-rank RNNs sampled from the same Gaussian weight distribution have the same mean field dynamics⁴⁶ albeit on differently oriented manifolds. Due to the arbitrary embedding of the manifolds across networks, we used geometry-agnostic MARBLE to produce feature embedding for 200 trials drawn from these three RNNs during stimulation ($E = 5$). We found the rotation-invariant features of the geometric-agnostic MARBLE is insensitive to the embedding of dynamics, i.e., plane orientation, and can uniquely detect a block diagonal structure in the distribution distance matrix across gain-modulated conditions, clearly discriminating between the on-manifold dynamics of networks sampled from Solution I and II while producing similar dynamics for the control (Fig. 2i, left). By contrast, canonical correlation analysis (CCA), which compares datasets based on point cloud-based representations, cannot detect dynamical changes because these occur within planes spanned by the same principal axes (Fig. 2i, right). This also suggests that previous methods that used CCA to detect changes across RNNs¹³ or animals^{4,48} could have detected the compound effect of changing manifold curvature and different sampling of state space, without concluding dynamical differences. In addition to correctly clustering solutions, the MDS embedding of the distance matrix (Fig. 2j) also shows that MARBLE reveals the underlying one-parameter variation due to gain modulation, which is correctly ordered within a network and across sampled networks. These findings confirm that our method can obtain a robust metric between dynamical processes generated by different system architectures with possible implications towards guiding their design for faster training or more accurate predictions.

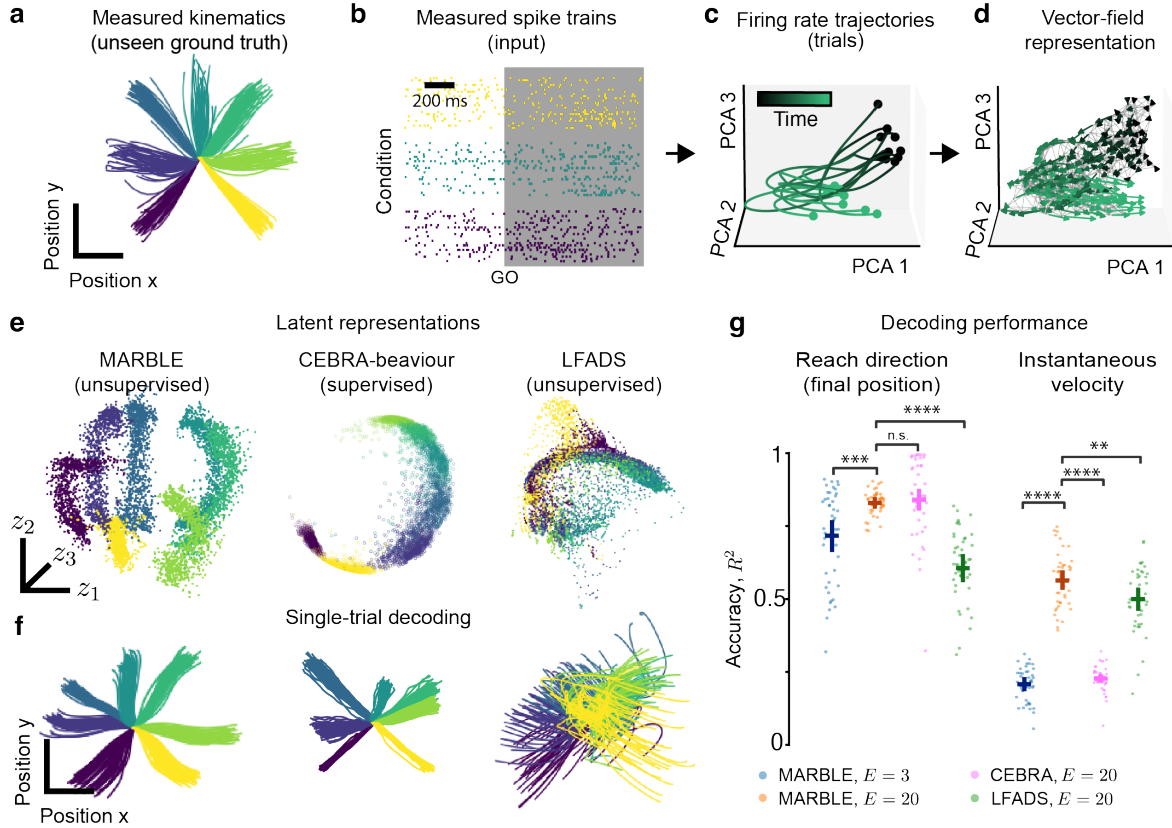


Figure 3: **Intepretable representation and decoding of neural activity in the prefrontal cortex in macaques during a centre-out reaching task.** **a** Ground truth hand trajectories in seven reaching directions. **b** Single-trial spike-trains in premotor cortex during a single trial for three respective reach directions (24 recording channels). The shaded area shows the analysed traces after the GO cue. **c** Ten representative firing rate trajectories for a given reach condition PCA-embedded in 3D for visualisation. **d** Vector field obtained from firing rate trajectories. **e** MARBLE embedding of neural data alone across conditions in a single session, compared with CEBRA (using reach conditions as labels) and LFADS. MARBLE embedding of neural dynamics for a given session geometrically corresponds to the reach configuration in physical space. **f** Linear decoding of hand trajectories from latent representations. **g** Decoding accuracy measured by R^2 between ground truth and decoded trajectories across all sessions for the final position (left) and instantaneous velocity (right). Wilcoxon tests (paired samples), **: $p < 1 \times 10^{-2}$, ***: $p < 1 \times 10^{-3}$, ****: $p < 1 \times 10^{-4}$. Horizontal and vertical bars show mean and one std, respectively.

Representing and decoding neural dynamics in a macaque reaching task

State-of-the-art representation-learning of neural dynamics uses a joint embedding of neural and behavioural signals³¹. However, true biological discovery should be based on post hoc interpretation of unsupervised representations rather than supervised learning based on pre-determined, user-defined condition labels. To exemplify this issue, we reanalysed electrophysiological recordings of a macaque performing a delayed centre-out hand-reaching task²⁷ (see Sect. S3.3 in the Material and Methods). During the task, a trained monkey was instructed to move a handle towards seven distinct targets placed at radial locations from the start position. This dataset comprises simultaneous recordings of hand kinematics (Fig. 3a) and neural activity via a 24-channel probe inserted into the premotor cortex (PMd) over 44 recording sessions (Fig. 3b shows one session).

Since a subset of neurons in PMd is directionally tuned⁴⁹, we argued that neural representations must be sensitive to the orientation of the neural manifold. For maximal expressivity, in this case, we trained a geometry-aware MARBLE network by constructing separate vector fields from the firing rate traces under individual reach conditions across which we expected the dynamics to be consistent (Fig. 3c-d). For comparison, we produced embeddings using two other prominent approaches: CE-

BRA [31], a supervised model using reach condition as labels (CEBRA-behaviour), and LFADS [27], an unsupervised model that uses generative recurrent neural networks. Our results show that the unsupervised MARBLE feature embeddings in 3D strongly reflect the spatial geometry of the physical reaches (Fig. 3e and Fig. S9a). By comparison, although the supervised CEBRA could partly unfold the arrangement of the reaches, the temporal evolution of trajectories was lost, and the latent factors from unsupervised LFADS lacked interpretability (Fig. 3e). The embeddings from point-wise methods such as PCA, t-SNE or UMAP showed similar loss of information (Fig. S8). This geometric configuration is also confirmed by the diagonal and periodic structure of the condition-averaged distance matrix between feature distributions across reach directions (Fig. S9b) and its associated MDS embedding (Fig. S9c). Hence, MARBLE can unfold global geometric information in the neural code that mirrors kinematics in physical space.

This interpretability based on a geometric correspondence between neural and behavioural representations suggests a potent decoding algorithm. To show this, we fitted an optimal linear estimator between the latent representations and their corresponding hand positions. Remarkably, the decoded kinematics showed excellent visual correspondence to ground truth kinematics both in directionality, comparable to supervised CEBRA and substantially better than unsupervised LFADS (Fig. 3f), quantified by a 10-fold cross-validated classification of final reach direction (Fig. 3g). Further, we find that while a three-dimensional ($E = 3$) MARBLE embedding accurately encodes spatial positions, the delay between the GO cue and the beginning of the movement could only be accounted for with higher embedding dimensions ($E = 20$, Fig. 3g). In this regard, MARBLE significantly outperformed both supervised CEBRA and LFADS models, which could not sufficiently unfold the latency and temporal variation of reaches to achieve linear decodability. These results highlight that MARBLE can generate representations of neural dynamics that are simultaneously interpretable and decodable into behavioural variables.

Consistent embeddings of neural dynamics across animals in the rat hippocampus

Recent evidence suggests there exists a strong similarity between neural representations across animals in a given task⁴⁸, with profound implications for, e.g., brain-machine interfacing. However, as shown above (Fig. 2i, Fig. S8), point-wise methods based on CCA¹³ and similar shape metrics^{13,14,44} do not capture dynamical variation that otherwise preserves the geometry of the neural manifold. While it is possible to ‘stitch’ multiple datasets by fitting auxiliary transformations²⁷ or aligning the neural dynamics to behaviour³¹, this relies on the assumption that the respective neurons encode the same computation.

Given that MARBLE can produce embeddings that are comparable across RNNs (Fig. 2h-i) and are interpretable within a given RNN (Fig. 2e-g) or animal (Fig. 3h-i), we finally asked whether it can produce consistently decodable embeddings across animals. To this end, we re-analysed electrophysiological recordings from the rat hippocampus during navigation of a linear track⁵⁰ (Fig. 4a, Sect. S3.4 in Materials and Methods). We found that from the neural data alone, MARBLE can infer interpretable representations consisting of a one-dimensional manifold in neural state space representing the animal’s position and walking direction (Fig. 4b). Remarkably, unsupervised MARBLE representations were significantly more interpretable than those obtained with CEBRA supervised by time labels alone (CEBRA-time) and comparable to providing both positional and directional information as labels (CEBRA-behaviour, Fig. 4b). This finding was corroborated by significantly higher decoding accuracy using a K-means decoder (Fig. 4c,d).

Finally, to demonstrate the consistency of MARBLE embeddings across animals, we aligned them post hoc using a linear transformation between animals. We found that the consistency, measured using the R^2 fit from a linear model trained using one animal as the target and one animal as the source, was significantly higher for unsupervised MARBLE than for self-supervised CEBRA-time, although not as good as supervised CEBRA-behaviour (Fig. 4e). This is remarkable given that MARBLE does not rely on external behavioural data yet finds consistent representations despite experimental and neurophysiological differences across animals. These findings underscore MARBLE’s potential for data-driven discovery and applications such as brain-computer interfaces.

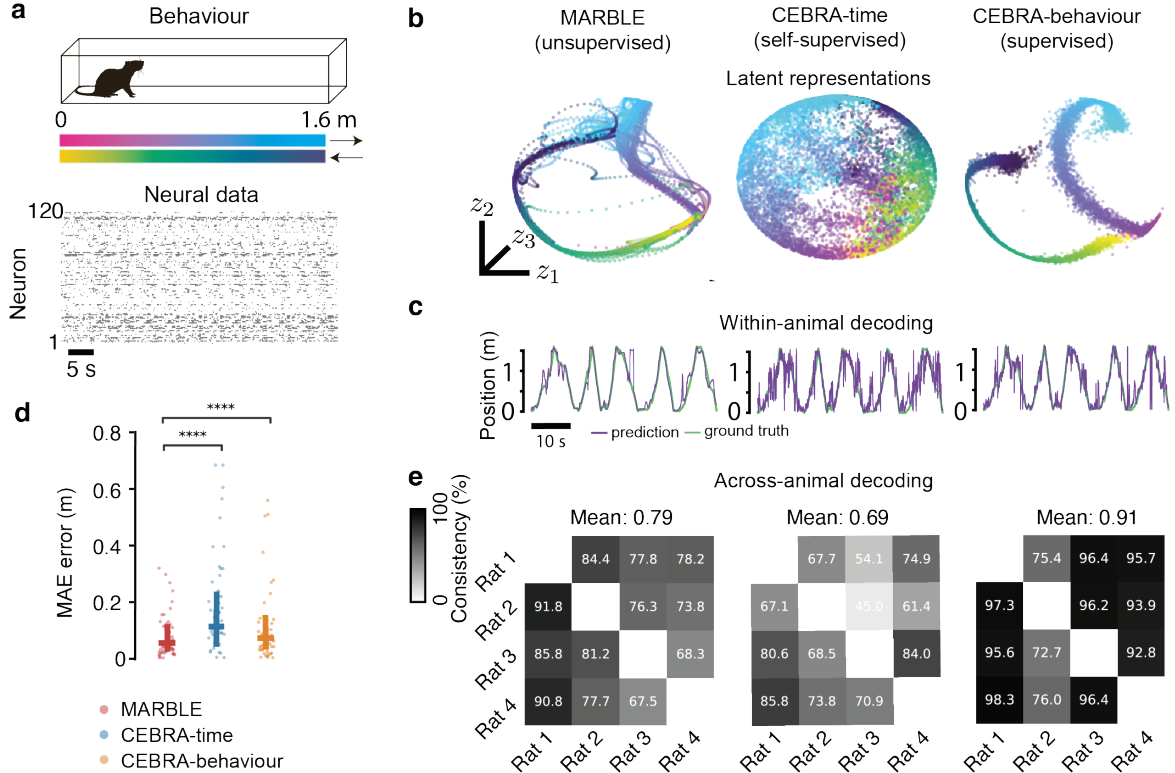


Figure 4: **Interpretable representation and cross-animal decoding of neural activity in rat hippocampus during linear maze navigation.** **a** Top: Experimental setup. Bottom: raster plot showing spiking activity in 120 neurons in a single session. **b** Comparison of latent representation ($E = 3$) of unsupervised MARBLE against self-supervised (time-only labels) and supervised (time, position and direction labels) CEBRA. **c** Time traces of linearly decoded animal position within Rat 1 ($E = 32$, default settings from CEBRA decoding notebook examples). **d** Decoding accuracy within the same animal. Wilcoxon tests (paired samples), ****: $p < 1 \times 10^{-4}$. Horizontal and vertical bars show mean and one std, respectively. **e** Cross-animal consistency as measured by R^2 of linear fit between the optimally aligned 3D embeddings of a source animal to a target animal.

Discussion

A hallmark of large collective systems such as the brain is the existence of many system realisations that lead to equivalent computations defined by population-level dynamical processes^{51,52}. The growing recognition that dynamics in biological and artificial neural networks evolve over low-dimensional manifolds^{5,6,8,9} offers an opportunity to reconcile the variability of dynamics across system realisations with the observed invariance of computations by using manifold geometry as an inductive bias for designing data-driven models. We have shown that non-linear dynamical systems can be represented as statistical distributions built from a point-wise, similarity-preserving embedding of local flow fields. Due to the continuity of the dynamics over the manifold, latent features can be learnt in a fully unsupervised manner using a geometric deep learning architecture. Further, features can be made rotation-invariant to achieve robust representations of perturbations in manifold geometry and orientation. These properties open the door to independently testing the relevance of manifold geometry and dynamics and comparing dynamics across system realisations.

Our formalism can be framed as a statistical generalisation of the convergent cross mapping (CCM) framework by Sugihara et al.³², which tests the topological equivalence of two dynamical attractors through a one-to-one map between their local neighbourhoods. CCM tests the causality between two long, concurrent time series without learning. In contrast, our method uses geometric deep learning to extract interpretable representations and provides a similarity metric between any collection of dynamical systems based on ensembles of variable-length, sparsely sampled time series. In addition, due to the locality of representations, our approach diverges from typical geometric deep learning

models that learn vector fields globally^{37,53} and are thus unable to consider the manifold geometry and the dynamics separately. Locality also implies that our method can generalise to assimilate different datasets without additional trainable parameters to increase the statistical power of the model even when individual datasets are poorly sampled. Although our method does not explicitly learn temporal dynamics over manifolds^{26,54}, we showed that temporal ordering naturally emerges from our similarity-preserving embeddings of local vector fields. We demonstrated that this property enables kinematic decoding from embeddings of neural data. Beyond their use in interpreting and decoding neural dynamics, we expect MARBLE embeddings to provide powerful representations for general machine-learning tasks, which is highly relevant to research in brain-machine interfaces.

Even though there is an increasing trend to jointly embed neural activity and behaviour to infer interpretable and consistent embeddings that do not suffer from 'nuisance variables', we have shown that MARBLE can uncover such embeddings from neural data alone. Hence, the LFF-based representations of neural dynamics obtained by MARBLE contain more behaviourally relevant information than neural data alone without the need for supervised learning using additional behavioural information to obtain comparable embeddings. This suggests a hypothesis that the neural readout into behaviour in biological brains might rely on the context of neural trajectories in a broader dynamical landscape.

Code availability

The code to carry out the simulations and analysis can be found at github.com/agosztolai/MARBLE.

Data availability

The data generated during the simulations is available with DOI: [10.7910/DVN/KTE4PC](https://doi.org/10.7910/DVN/KTE4PC).

Acknowledgements

We thank Nicolas Aspert for the much-needed computing support. We also thank Adrian Valente, Nikolas Karalias and Matteo Vinao-Carl for the interesting discussions. AG acknowledges support from an HFSP Cross-disciplinary Postdoctoral Fellowship (LT000669/2020-C). MB acknowledges funding through EPSRC awards EP/N014529/1 (Centre for Mathematics of Precision Healthcare) and EP/W024020/1 (Statistical Physics of Cognition). RP acknowledges the Deutsche Forschungsgemeinschaft (DFG, German Research Foundation) Project-ID 424778381-TRR 295. A.A. was supported by funding to the Blue Brain Project, a research centre of the École polytechnique fédérale de Lausanne (EPFL), from the Swiss government's ETH Board of the Swiss Federal Institutes of Technology.

Author contributions

Conceptualisation: A.G., R.L.P., A.A., M.B., P.V., Methodology: A.G., R.L.P., A.A., P.V., Software: A.G., R.L.P., A.A., Analysis: A.G., R.L.P., A.A., Writing - Original Draft: A.G., R.L.P., A.A., Writing - Review & Editing: M.B., P.V.

Competing interests

The authors declare no competing interests.

References

1. Hopfield, J. J. Neural networks and physical systems with emergent collective computational abilities. *Proc. Natl. Acad. Sci. U. S. A.* **79**, 2554–2558 (1982).

2. Churchland, M. M. *et al.* Neural population dynamics during reaching. *Nature* **487**, 51–56 (2012).
3. Vyas, S. *et al.* Computation through Neural Population Dynamics. *Annu. Rev. Neurosci.* **43**, 249–275 (2020).
4. Gallego, J. A. *et al.* Neural manifolds for the control of movement. *Neuron* **94**, 978–984 (2017).
5. Chung, S., Lee, D. D. & Sompolinsky, H. Classification and geometry of general perceptual manifolds. *Phys. Rev. X* **8**, 31003 (2018).
6. Chaudhuri, R. *et al.* The intrinsic attractor manifold and population dynamics of a canonical cognitive circuit across waking and sleep. *Nat. Neurosci.* **22**, 1512–1520 (2019).
7. Kriegeskorte, N. & Wei, X.-X. Neural tuning and representational geometry. *Nat. Rev. Neurosci.* **22**, 703–718 (2021).
8. Khona, M. & Fiete, I. R. Attractor and integrator networks in the brain. *Nat. Rev. Neurosci.* **23**, 744–766 (2022).
9. Gardner, R. J. *et al.* Toroidal topology of population activity in grid cells. *Nature* **602**, 123–128 (2022).
10. Nogueira, R. *et al.* The geometry of cortical representations of touch in rodents. *Nat. Neurosci.* **26**, 239–250 (2023).
11. Beiran, M. *et al.* Parametric control of flexible timing through low-dimensional neural manifolds. *Neuron* **111**, 739–753.e8 (2023).
12. Langdon, C., Genkin, M. & Engel, T. A. A unifying perspective on neural manifolds and circuits for cognition. *Nat. Rev. Neurosci.* (2023).
13. Maheswaranathan, N. *et al.* Universality and individuality in neural dynamics across large populations of recurrent networks. *Adv. Neural Inf. Process. Syst.* **32** (2019).
14. Williams, A. H. *et al.* Generalized shape metrics on neural representations. *Adv. Neural Inf. Process. Syst.* **6**, 4738–4750 (2021).
15. Sussillo, D. & Barak, O. Opening the black box: low-dimensional dynamics in high-dimensional recurrent neural networks. *Neural Comput.* **25**, 626–649 (2013).
16. Duncker, L. & Sahani, M. Dynamics on the manifold: Identifying computational dynamical activity from neural population recordings. *Curr. Opin. Neurobiol.* **70**, 163–170 (2021).
17. Peach, R. L. *et al.* *Implicit Gaussian process representation of vector fields over arbitrary latent manifolds* 2023. arXiv: [2309.16746](https://arxiv.org/abs/2309.16746) [cs.LG].
18. Toi, P. T. *et al.* In vivo direct imaging of neuronal activity at high temporospatial resolution. *Science* **378**, 160–168 (2022).
19. Steinmetz, N. A. *et al.* Neuropixels 2.0: A miniaturized high-density probe for stable, long-term brain recordings. *Science* **372**, eabf4588 (2021).
20. Villette, V. *et al.* Ultrafast Two-Photon Imaging of a High-Gain Voltage Indicator in Awake Behaving Mice. *Cell* **179**, 1590–1608.e23 (2019).
21. Van der Maaten, L. & Hinton, G. Visualizing Data using t-SNE. *Journal of Machine Learning Research* **9**, 2579–2605. <http://jmlr.org/papers/v9/vandermaaten08a.html> (2008).
22. McInnes, L. *et al.* UMAP: Uniform Manifold Approximation and Projection. *The Journal of Open Source Software* **3**, 861 (2018).
23. Brunton, S. L. *et al.* Chaos as an intermittently forced linear system. *Nat. Commun.* **8**, 1–8 (2017).
24. Lusch, B., Kutz, J. N. & Brunton, S. L. Deep learning for universal linear embeddings of nonlinear dynamics. *Nat. Commun.* **9**, 851–10 (2018).
25. Kipf, T. *et al.* Neural Relational Inference for Interacting Systems. *arXiv preprint arXiv:1802.04687* (2018).
26. Low, R. J. *et al.* Probing variability in a cognitive map using manifold inference from neural dynamics. *bioRxiv* (2018).

27. Pandarinath, C. *et al.* Inferring single-trial neural population dynamics using sequential auto-encoders. *Nat. Methods*, 1–21 (2018).
28. Zhu, F. *et al.* A deep learning framework for inference of single-trial neural population dynamics from calcium imaging with subframe temporal resolution. *Nat. Neurosci.* **25**, 1724–1734 (2022).
29. Stroud, J. P. *et al.* Motor primitives in space and time via targeted gain modulation in cortical networks. *Nat. Neurosci.* **21**, 1774–1783 (2018).
30. Zhou, D. & Wei, X.-X. *Learning identifiable and interpretable latent models of high-dimensional neural activity using pi-VAE* 2020. arXiv: [2011.04798 \[stat.ML\]](https://arxiv.org/abs/2011.04798).
31. Schneider, S., Lee, J. H. & Mathis, M. W. Learnable latent embeddings for joint behavioural and neural analysis. *Nature* **617**, 360–368 (2023).
32. Sugihara, G. *et al.* Detecting causality in complex ecosystems. *Science (80-.)*. **338**, 496–500 (2012).
33. Gosztojai, A. & Arnaudon, A. Unfolding the multiscale structure of networks with dynamical Ollivier-Ricci curvature. *Nat. Commun.* **12**, 4561 (2021).
34. Skinner, D. J. *et al.* Topological metric detects hidden order in disordered media. *Phys. Rev. Lett.* **126**, 48101 (2021).
35. Sharp, N. *et al.* DiffusionNet : discretization agnostic learning on surfaces. *ACM Trans. Graph.* **99** (2020).
36. Beaini, D. *et al.* *Directional graph networks* in *International Conference on Machine Learning* (2021), 748–758.
37. Bodnar, C. *et al.* *Neural Sheaf Diffusion: A topological perspective on heterophily and over-smoothing in GNNs* in *Advances in Neural Information Processing Systems* (eds Oh, A. H. *et al.*) (2022).
38. Hamilton, W. L., Ying, R. & Leskovec, J. Inductive representation learning on large graphs. *Adv. Neural Inf. Process. Syst.* **2017-Decem**, 1025–1035 (2017).
39. Fefferman, C., Mitter, S. & Narayanan, H. Testing the manifold hypothesis. *Journal of the American Mathematical Society* **29**, 983–1049 (2016).
40. Sugihara, G. & May, R. M. Nonlinear forecasting as a way of distinguishing chaos from measurement error in time series. *Nature* **344**, 734–741 (1990).
41. Flesch, T. *et al.* Orthogonal representations for robust context-dependent task performance in brains and neural networks. *Neuron* **110**, 1258–1270.e11 (2022).
42. Rajalingham, R., Piccato, A. & Jazayeri, M. Recurrent neural networks with explicit representation of dynamic latent variables can mimic behavioral patterns in a physical inference task. *Nat. Commun.* **13** (2022).
43. Galgali, A. R., Sahani, M. & Mante, V. Residual dynamics resolves recurrent contributions to neural computation. *Nat. Neurosci.* (2023).
44. Kornblith, S. *et al.* Similarity of neural network representations revisited. *36th Int. Conf. Mach. Learn. ICML 2019* **2019-June**, 6156–6175 (2019).
45. Miyashita, Y. Neuronal correlate of visual associative long-term memory in the primate temporal cortex. *Nature* **335**, 817–820 (1988).
46. Dubreuil, A. *et al.* The role of population structure in computations through neural dynamics. *Nat. Neurosci.* **25**, 783–794 (2022).
47. Mastrogiuseppe, F. & Ostojic, S. Linking Connectivity, Dynamics, and Computations in Low-Rank Recurrent Neural Networks. *Neuron* **99**, 609–623.e29 (2018).
48. Safaie, M. *et al.* Preserved neural dynamics across animals performing similar behaviour. *Nature* **623** (2023).
49. Riehle, A. & Requin, J. Monkey primary motor and premotor cortex: single-cell activity related to prior information about direction and extent of an intended movement. *Journal of Neurophysiology* **61**, 534–549 (1989).

50. Groszmark, A. D. & Buzsáki, G. Diversity in neural firing dynamics supports both rigid and learned hippocampal sequences. *Science (80-.)*. **351**, 1440–1443 (Mar. 2016).
51. Marder, E. & Taylor, A. L. Multiple models to capture the variability in biological neurons and networks. *Nat. Neurosci.* **14**, 133–138 (2011).
52. Gosztołai, A. & Ramdya, P. Connecting the dots in ethology: applying network theory to understand neural and animal collectives. *Curr. Opin. Neurobiol.* **73**, 102532 (2022).
53. Grattarola, D. & Vandergheynst, P. Generalised implicit neural representations. *Advances in Neural Information Processing Systems* (2022).
54. Floryan, D. & Graham, M. D. Data-driven discovery of intrinsic dynamics. *Nat. Mach. Intell.* **4**, 1113–1120 (2022).
55. Mount, D. M. & Arya, S. Finding the nearest neighbors for points in d-dimensional Euclidean space. *ACM Transactions on Mathematical Software (TOMS)* **24**, 96–103 (1998).
56. Berry, T. & Sauer, T. Consistent manifold representation for topological data analysis. *Foundations of Data Science* **1**, 1–38 (2019).
57. Budninskiy, M. *et al.* Parallel Transport Unfolding: A Connection-Based Manifold Learning Approach. *SIAM Journal on Applied Algebra and Geometry* **3**, 266–291 (2019).
58. Kabsch, W. A solution for the best rotation to relate two sets of vectors. *Acta Crystallographica Section A* **32**, 922–923 (Sept. 1976).
59. Berline N. Getzler E., V. M. *Heat kernels and Dirac operators* 2nd. (Springer, 1996).
60. Singer, A. & Wu, H. T. Vector diffusion maps and the connection Laplacian. *Commun. Pure Appl. Math.* **65**, 1067–1144 (2012).
61. He, K. *et al.* *Deep Residual Learning for Image Recognition in 2016 IEEE Conference on Computer Vision and Pattern Recognition (CVPR)* (2016), 770–778.
62. Fey, M. & Lenssen, J. E. *Fast Graph Representation Learning with PyTorch Geometric in ICLR Workshop on Representation Learning on Graphs and Manifolds* (2019).
63. Kingma, D. P. & Ba, J. *Adam: A Method for Stochastic Optimization* 2014.
64. Denker, M., Yegenoglu, A. & Grün, S. *Collaborative HPC-enabled workflows on the HBP Collaboratory using the Elephant framework in Neuroinformatics 2018* (2018), P19.

Supplementary Material for: Interpretable statistical representations of neural population dynamics and geometry

Adam Gosztolai,^{1*} Robert L. Peach,^{2,3} Alexis Arnaudon,⁴
Mauricio Barahona,⁴ Pierre Vanderghelynst¹

¹Signal Processing Laboratory (LTS2), EPFL, Lausanne, 1016, Switzerland

²Department of Neurology, University Hospital Würzburg, Würzburg, 97070, Germany

³Department of Brain Sciences, Imperial College London, London, W12 0NN, United Kingdom,

⁴Department of Mathematics, Imperial College London, London, SW7 2AZ, United Kingdom

*To whom correspondence should be addressed; E-mail: adam.gosztolai@epfl.ch.

S1 The MARBLE method

The MARBLE method aims to find a similarity-preserving map from the local flow fields (LFFs) to a shared latent space. Since the method processes vector fields point-by-point, it suffices to describe it applied on a single manifold and associated dynamical flows obtained from an ensemble of trials. The generalisation of the method to the joint embedding of multiple vector fields is immediate.

Given a smooth, compact m -dimensional submanifold \mathcal{M} of \mathbb{R}^d described by a point cloud $\mathbf{X} = (\mathbf{x}_1, \dots, \mathbf{x}_n)$, MARBLE aims at representing the discrete vector field $\mathbf{F} = \{\mathbf{f}_1, \dots, \mathbf{f}_n\}$ supported over the point cloud as an empirical distribution $P(\mathbf{Z}) = \sum_{i=0}^n \delta(\mathbf{z}_i)$ of latent features $\mathbf{Z} = (\mathbf{z}_1, \dots, \mathbf{z}_n)$. The vectors $\{\mathbf{f}_i\}$ can be obtained from time-series data, for example, by taking first-order finite differences $\mathbf{f}_i := \mathbf{x}(t_i + 1) - \mathbf{x}(t_i)$. We now introduce an unsupervised geometric deep learning architecture for obtaining the latent features $\{\mathbf{z}_i\}$ based on the vector field restricted to a neighbourhood around each point $\{\mathbf{x}_i\}$.

S1.1 Approximating the manifold by a proximity graph

To define the locality on \mathcal{M} , we describe it with a proximity graph. We must ensure that the graph is as homogeneous as possible to obtain a faithful representation of the tangent space of \mathcal{M} via the vector field \mathbf{F} . In particular, consecutive temporal points over dynamical trajectories should not be overrepresented in neighbourhoods of any point relative to points in close trajectories. For this reason, we generate the proximity graph from a subsample of points obtained by farthest point sampling⁵⁵, with a criterion $\delta \in [0, 1]$ that controls the spacing of the points relative to the diameter of the manifold $\max_{i,j}(\|\mathbf{x}_i - \mathbf{x}_j\|_2) < \delta \text{diam}(\mathcal{M})$.

Several proximity graph algorithms can be used, such as the k -NN algorithm and the ϵ -ball algorithm, but we found that the continuous k -nearest neighbour (ck -NN) algorithm⁵⁶ creates more representative neighbourhoods. Indeed, contrary to the classical k -NN graph algorithm, it can be interpreted as a local kernel density estimate and accounts for sampling density variations over \mathcal{M} . The ck -NN algorithm extends the classical k -NN algorithm by accounting for density variations by connecting i and j whenever $\|\mathbf{x}_i - \mathbf{x}_j\|_2^2 < \delta \|\mathbf{x}_i - \mathbf{x}_u\|_2 \|\mathbf{x}_j - \mathbf{x}_v\|_2$, where $\delta > 0$ is a scaling parameter, u, v are the k -th nearest neighbours of i, j , respectively, and $\|\cdot\|_2$ is the Euclidean norm. This proximity graph endows \mathcal{M} with a geodesic structure, i.e., for any $i, j \in \mathcal{M}$, there is a shortest path with distance $d(i, j)$. We can then define the local vector fields as the p -hop geodesic neighbourhood $\mathcal{N}(i, p)$ around each point i .

S1.2 Parametrising the tangent spaces

The tangent spaces of \mathcal{M} do not have a preferred coordinate system. However, being isomorphic to \mathbb{R}^m , $\mathcal{T}_i\mathcal{M}$ can be parametrised by m orthogonal vectors in the ambient space \mathbb{R}^d to form a local frame or gauge. Specifically, we assume that the tangent space at a node i , $\mathcal{T}_i\mathcal{M}$, is spanned by the edge vectors $\mathbf{e}_{ij} \in \mathbb{R}^d$ pointing from i to K nodes j in its neighbourhood on the proximity graph. The m largest singular values $\mathbf{t}_i^{(\cdot)} \in \mathbb{R}^d$ of the matrix formed by column-stacking \mathbf{e}_{ij} yield the orthonormal coordinate frame $\mathbb{T}_i \in \mathbb{R}^{d \times m} = (\mathbf{t}_i^{(1)}, \dots, \mathbf{t}_i^{(m)})$ spanning $\mathcal{T}_i\mathcal{M}$. In practice, we pick $K > \text{deg}(i)$ closest nodes to i on the proximity graph where K is a hyperparameter. Larger K increases the overlaps between the nearby tangent spaces, and we find that $K = 2|\mathcal{N}(i, 1)|$ is often a good compromise between locality and robustness to noise of the tangent space approximation. Note that because \mathbb{T}_i defines an orthogonal basis, $\mathbb{T}_i^T \mathbf{f}_i$ acts as a projection of the signal to the tangent space in the ℓ_2 sense. We perform these computations using a modified Parallel Transport Unfolding package⁵⁷. We illustrate the computed frames on a spherical manifold (Fig. S1).

S1.3 Connections between tangent spaces

Having the local frames, we next define the parallel transport map $\mathcal{P}_{j \rightarrow i}$ aligning the local frame at j to that at i , which is necessary to define convolution operations in a common space. While parallel transport is generally path dependent, we assume that adjacent nodes i, j are close enough to consider the unique smallest rotation, known as the Lévy-Civita connection. Thus, for adjacent edges, $\mathcal{P}_{j \rightarrow i}$ can be computed as the matrix \mathbf{O}_{ji} corresponding to $\mathcal{P}_{j \rightarrow i}$, as the orthogonal transformation (rotation and reflection)

$$\mathbf{O}_{ji} = \arg \min_{\mathbf{O} \in O(m)} \|\mathbb{T}_i - \mathbb{T}_j \mathbf{O}\|_F, \quad (\text{S1})$$

where $\|\cdot\|_F$ is the Frobenius norm. The unique solution to this problem is found by the Kabsch algorithm⁵⁸.

Note that \mathbb{T}_i is defined only up to an orthogonal transformation (rotation and reflection) within the tangent space of \mathcal{M} because the m -dimensional $\mathcal{T}_i\mathcal{M}$ only constrains m coordinates of the frame. However, when the signal is projected to the local frame, the tangent frame alignment by $\mathcal{P}_{j \rightarrow i} = \mathbf{O}_{ij}$ removes this ambiguity. Indeed, suppose that each node carries the same signal \mathbf{f} , then, parallel transport alignment of the projected signal from j to i yields

$$\mathbb{T}_i^T \mathbf{f} = \mathbf{O}_{ij} \mathbb{T}_j^T \mathbf{f} = (\mathbb{T}_j \mathbf{O}_{ji})^T \mathbf{f} = \mathbb{T}_i^T \mathbf{f}, \quad (\text{S2})$$

where the first equality used the definition of the parallel transport, the second equality used the transpose operation, while the third equality used Eq. S1. Note that the same result does not hold when parallel transporting signals in the ambient space (without projection) because, in that case, the ambiguity in the frame orientation introduces ambiguity in the signal

S1.4 Vector diffusion

Before constructing the vector field features, we use a vector diffusion layer to smooth out noisy vector field samples. Vector diffusion is a generalisation of the scalar (heat) diffusion and can be expressed as a kernel associated with the vector diffusion equation⁵⁹ to produce a smoothed vector field

$$\text{vec}(\mathbf{F}(\tau)) = e^{-\tau \mathcal{L}} \text{vec}(\mathbf{F}), \quad (\text{S3})$$

where $\text{vec}(\mathbf{F}) \in \mathbb{R}^{nm \times 1}$ the row-wise concatenation of vector-valued signals, τ is a learnable parameter that controls the scale of the local vector fields and \mathcal{L} is the random-walk normalised connection Laplacian defined as a block matrix whose nonzero blocks are given by

$$\mathcal{L}(i, j) = \begin{cases} \mathbf{I}_{m \times m} & \text{for } i = j \\ -\text{deg}(i)^{-1} \mathbf{O}_{ij} & \text{for } j \in \mathcal{N}(i, 1). \end{cases} \quad (\text{S4})$$

See⁶⁰ for further details. Intuitively, rather than diffusion of the vectors component-wise, vector diffusion smoothens vectors based on differences between a vector at a given node and other vectors parallel transported to this node.

S1.5 Gradient filters

Before we can learn the vector field features, we define gradient filters, whose role is to approximate the variation of the vector field around a point in the local tangent frame. To numerically compute the gradient at a point $i \in \mathcal{M}$ we construct an anisotropic filter by extending the directional derivative filter of³⁶ using local coordinates. To do so, consider the local frame \mathbb{T}_i and construct the directional derivative filter in the direction of the q -th unit vector $\mathbf{t}_i^{(q)}$. We follow³⁶ and decompose $\mathbf{t}_i^{(q)} \in \mathbb{R}^{d \times 1}$ by projecting it to the set of edge vectors \mathbf{e}_{ij} to obtain a vector $\hat{\mathbf{t}}_i^{(q)} \in \mathbb{R}^{n \times 1}$ at node i pointing in the basis direction q with components j

$$\hat{\mathbf{t}}_i^{(q)}(j) = \begin{cases} \langle \mathbf{t}_i^{(q)}, \mathbf{e}_{ij} \rangle / \text{deg}(i) & \text{if } j \in \mathcal{N}(i, 1) \\ 0 & \text{otherwise.} \end{cases} \quad (\text{S5})$$

Collating for all nodes, we can write a matrix for the q -th coordinate of the local frame projected onto the edge vectors $\hat{\mathbb{T}}_q = (\hat{\mathbf{t}}_1^{(q)}, \dots, \hat{\mathbf{t}}_n^{(q)}) \in \mathbb{R}^{n \times n}$. Using this decomposition, the directional derivative of the scalar field s_i at i in the direction \mathbf{t}_i^q is given by

$$\mathcal{K}^{(i,q)} s_i := \langle \nabla s_i, \hat{\mathbf{t}}_i^{(q)} \rangle = \sum_{j \in \mathcal{N}(i,1)} (s_j - s_i) \hat{\mathbf{t}}_i^{(q)}(j), \quad (\text{S6})$$

or, in matrix form, by

$$\mathbf{K}^{(q)} \mathbf{s} = (\hat{\mathbb{T}}_q - \text{diag}(\hat{\mathbb{T}}_q \mathbf{1}_n)) \mathbf{s}, \quad (\text{S7})$$

where $\mathbf{1}_n$ is the $n \times 1$ vector of ones. As a result, the gradient of a scalar field can be obtained by column-wise concatenating (as new channels) the derivatives against all directions in the basis set

$$\nabla \mathbf{s} = (\mathcal{D}^{(1)} \mathbf{s}, \dots, \mathcal{D}^{(d)} \mathbf{s}). \quad (\text{S8})$$

Figs. S2a,b show the output of the first and second-order filters applied to a linear and a quadratic scalar field.

To compute the component-wise directional derivative for a vector field $\mathbf{F} \in \mathbb{R}^{n \times m}$, one must first parallel transport the local frames at the neighbours j to i before applying the anisotropic filters in Eq. S7. Let \mathbf{O} denote the $nm \times nm$ block matrix of $m \times m$ blocks given by the connection matrices \mathbf{O}_{ij} . Then, we may express Eq. S12 in matrix form as

$$\mathcal{D}^{(q)} \mathbf{F} = ((\mathbf{K}^{(q)} \otimes \mathbf{1}_m^T \mathbf{1}_m) \odot \mathbf{O}) \mathbf{F}. \quad (\text{S9})$$

Here the kronecker product in the inner brackets expands $\mathbf{K}^{(q)}$ to the $nm \times nm$ block matrix where the (i, j) $m \times m$ block is filled with entries $K_{ij}^{(q)}$.

S1.6 Approximating local vector fields

We now define convolution kernels on \mathcal{M} that act on the vector field to represent the vector field around a given point. We first project the vector signal to the manifold $\mathbf{f}'_i = \mathbb{T}_i^T \mathbf{f}_i$. This reduces the dimension of \mathbf{f}_i from d to m without losing information since \mathbf{f}_i was already in the tangent space. We drop the bar in the sequel to understand that all vectors are expressed in local coordinates. In this local frame, the best polynomial approximation of the vector field around i is given by the Taylor-series expansion of each component $f_{i,l}$ of \mathbf{f}_i

$$f_{j,l} \approx f_{i,l} + \nabla f_{i,l} (\mathbf{x}_j - \mathbf{x}_i) + \frac{1}{2} (\mathbf{x}_j - \mathbf{x}_i)^T \nabla^2 f_{i,l} (\mathbf{x}_j - \mathbf{x}_i) + \dots \quad (\text{S10})$$

Motivated by the Taylor approximation, we construct gradient operators of increasing order and implement them as a set of m anisotropic filters $\{\mathcal{D}^{(a)}\}$ acting along $\{\mathbf{t}_i^{(a)}\}$,

$$\nabla f_{i,l} \approx \left(\mathcal{D}^{(1)}(f_{i,l}), \dots, \mathcal{D}^{(m)}(f_{i,l}) \right)^T. \quad (\text{S11})$$

Here, $\mathcal{D}^{(a)}(f_{i,l})$ is the l -th component of

$$\mathcal{D}^{(a)}(\mathbf{f}_i) = \sum_{j=1}^n \mathcal{K}_j^{(i,q)} \mathcal{P}_{j \rightarrow i}(\mathbf{f}_j), \quad (\text{S12})$$

where $\mathcal{P}_{j \rightarrow i} = \mathbf{O}_{ij}$ is the parallel transport operator that takes the vector \mathbf{f}_j from the adjacent frame j to a common frame at i . $\mathcal{K}^{(i,q)} \in \mathbb{R}^{n \times n}$ is a directional derivative filter³⁶ (Eq. S7) expressed in local coordinates at i and acting along $\mathbf{t}_i^{(q)}$. As a result of the parallel transport, the value of Eq. S12 is independent of the local curvature of the manifold. The p -th order gradients can be defined by the iterated application of the filters, which aggregates information in the p -hop neighbourhood of points. Although we find that increasing the order of the differential operators increases the expressiveness of the network (Fig. S3), second-order filters ($p = 2$) were sufficient for the application considered in this paper.

The expansion in Eq. S10 suggests augmenting the vectors \mathbf{f}_i by the derivatives (Eq. S11), to obtain a matrix

$$\mathbf{f}_i \mapsto \mathbf{f}_i^{\mathcal{D}} = (\mathbf{f}_i, \nabla f_{i,1}, \dots, \nabla f_{i,m}, \nabla(\nabla f_{i,1})_1, \dots, \nabla(\nabla f_{i,m})_m), \quad (\text{S13})$$

of dimensions $m \times c$ whose columns are gradients of signal components up to order p to give a total of $c = (1 - m^{p+1})/(m(1 - m))$ vectorial channels.

S1.7 Inner product for geometry invariance

In the optional geometry-agnostic mode, deformations on the manifold have the effect of introducing rotations into the local vector fields. Thus, we can achieve invariance to these deformations by making the learnt features rotation invariant. We do so by first transforming the $m \times c$ matrix $\mathbf{f}_i^{\mathcal{D}}$ to a $1 \times c$ vector as

$$\mathbf{f}_i^{\mathcal{D}} \mapsto \mathbf{f}_i^{\text{ip}} = (\mathcal{E}^{(1)}(\mathbf{f}_i^{\mathcal{D}}), \dots, \mathcal{E}^{(c)}(\mathbf{f}_i^{\mathcal{D}})). \quad (\text{S14})$$

Then, by taking for each channel the inner product against all other channels, weighted by a dense learnable matrix $\mathbf{A}^{(r)} \in \mathbb{R}^{m \times m}$ and summing, we obtain

$$\mathcal{E}^{(r)}(\mathbf{f}_i^{\mathcal{D}}) = \mathcal{E}^{(r)}(\mathbf{f}_i^{\mathcal{D}}; \mathbf{A}^{(r)}) := \sum_{s=1}^c \left\langle \mathbf{f}_i^{\mathcal{D}}(\cdot, r), \mathbf{A}^{(r)} \mathbf{f}_i^{\mathcal{D}}(\cdot, s) \right\rangle, \quad (\text{S15})$$

for $r = 1, \dots, c$ (Fig. 1f). Taking inner products is valid because the columns of $\mathbf{f}_i^{\mathcal{D}}$ all live in the tangent space at i . Intuitively, Eq. S15 achieves coordinate independence by learning rotation and scaling relationships between pairs of channels.

S1.8 Embedding with a multilayer perceptron (MLP)

To embed each local feature, \mathbf{f}_i^{ip} or $\mathbf{f}_i^{\mathcal{D}}$, depending on if inner product features are used, (Eq. S14) we use a multilayer perceptron (MLP) (Fig. 1g)

$$\mathbf{z}_i = \text{MLP}(\mathbf{f}_i^{\text{ip}}; \omega), \quad (\text{S16})$$

where ω are trainable weights. The MLP is composed of L linear (fully-connected) layers interspersed by ReLU non-linearities. We used $L = 2$ with a sufficiently high output dimension to encode the variables of interest. The parameters were initialised using the Kaiming method⁶¹.

S1.9 Loss function

Unsupervised training of the network is possible due to the continuity in the vector field over \mathcal{M} , which causes nearby local vector fields to be more similar than distant ones. We implement this via negative sampling³⁸, which uses random walks sampled at each node to embed neighbouring points on the manifold close together while pushing points sampled uniformly at random far away. We use the following unsupervised loss function³⁸

$$\mathcal{J}(\mathbf{Z}) = -\log(\sigma(\mathbf{z}_i^T \mathbf{z}_j)) - Q \mathbb{E}_{k \sim U(n)} \log(\sigma(-\mathbf{z}_i^T \mathbf{z}_k)), \quad (\text{S17})$$

where $\sigma(x) = (1 + e^{-x})^{-1}$ is the sigmoid function and $U(n)$ is the uniform distribution over the n nodes. To compute this function, we sample one-step random walks from every node i to obtain 'positive' node samples for which we expect similar local vector fields to that of node i . The first term in Eq. S17 seeks to embed these nodes close together. At the same time, we also sample nodes

uniformly at random to obtain 'negative' node samples with likely different local vector fields from that of node i . The second term in Eq. S17 seeks to embed these nodes far away. We also choose $Q = 1$.

We optimise the loss Eq. S17 by stochastic gradient descent. For training, the nodes from all manifolds were randomly split into training (80%), validation (10%) and test (10%) sets. The optimiser was run until convergence of the validation set and the final results were tested on the test set with the optimised parameters.

S1.10 Pseudo code of MARBLE algorithm

We implemented MARBLE architecture with Pytorch Geometric⁶². The general algorithm is as follows.

Algorithm 1 MARBLE

Input: d -dimensional vector field samples $\mathbf{F} = (\mathbf{f}_1, \dots, \mathbf{f}_n)$

connection Laplacian \mathcal{L}

derivative filters $\mathcal{D}_i^{(q)}$ for $i \in \{1, \dots, n\}$ and $q \in \{1, \dots, m\}$

derivative order p

Output: Embedding \mathbf{z}_i for all $i \in \{1, \dots, n\}$

$\mathbf{F} \leftarrow e^{\tau \mathcal{L}} \mathbf{F}$ ▷ Apply diffusion layer (optional)

$\mathbf{h}^{(0)} \leftarrow \mathbf{f}_i$

for $1 \leq l \leq p$ **do** ▷ Loop over filter orders

$\nabla h_q^{(l)} = \left(\mathcal{D}^{(1)}(h_q^{(l)}), \dots, \mathcal{D}^{(m)}(h_q^{(l)}) \right)^T$ ▷ Compute filters

$\mathbf{h}^{(l)} \leftarrow \text{concat} \left(\mathbf{h}^{(l-1)}, \nabla h_1^{(l)}, \dots, \nabla h_m^{(l)} \right)$ ▷ Concatenate derivatives

end for

$\mathbf{h}^{(l)} \leftarrow (\mathcal{E}_1(\mathbf{h}^{(l)}; \mathbf{A}_1), \dots, \mathcal{E}_c(\mathbf{h}^{(l)}; \mathbf{A}_c))$ ▷ Inner product features (optional)

$\mathbf{z}_i \leftarrow \text{MLP}(\mathbf{h}^{(l)}; \omega)$ ▷ Pass through MLP

S2 Distributional distance between latent representations

To test whether shifts in the statistical representation of the dynamical system can predict global phenomena in the dynamics we define a similarity metric between pairs of vector fields $\mathbf{F}_1, \mathbf{F}_2$ with respect to their corresponding embeddings $\mathbf{Z}_1 = (\mathbf{z}_{1,1}, \dots, \mathbf{z}_{n_1,1})$ and $\mathbf{Z}_2 = (\mathbf{z}_{1,1}, \dots, \mathbf{z}_{n_2,1})$. We use the optimal transport distance between the empirical distributions $P_1 = \sum_i^{n_1} \delta(\mathbf{z}_{i,1}), P_2 = \sum_i^{n_2} \delta(\mathbf{z}_{i,2})$

$$d(P_1, P_2) = \min_{\gamma} \sum_{uv} \gamma_{uv} \|\mathbf{z}_{u,1} - \mathbf{z}_{v,2}\|_2^2, \quad (\text{S18})$$

where γ is the transport plan, a joint probability distribution subject to marginality constraints that $\sum_u \gamma_{uv} = P_2, \sum_v \gamma_{uv} = P_1$ and $\|\cdot\|_2$ is the Euclidean distance.

S3 Examples

We give here more details on the examples of the main text.

S3.1 Van der Pol oscillator on paraboloid

We used the following equations to simulate the Van der Pol system:

$$\begin{aligned} \dot{x} &= y \\ \dot{y} &= \mu(1 - x^2)y - x, \end{aligned} \quad (\text{S19})$$

parametrised by μ . If $\mu = 0$, the system reduces to the harmonic oscillator, if $\mu < 0$, the system is unstable and if $\mu > 0$, the system is stable and converges to a limit cycle. In addition, we map this two-dimensional system to a paraboloid as with the map

$$\begin{aligned} x, y &\mapsto x, y, z = \text{parab}(x, y) \\ \dot{x}, \dot{y} &\mapsto \dot{x}, \dot{y}, \dot{z} = \text{parab}(x + \dot{x}, y + \dot{y}) - \text{parab}(x, y), \end{aligned}$$

where $\text{parab}(x, y) = -(\alpha x)^2 - (\alpha y)^2$.

We sought to test whether we can distinguish on-manifold dynamical variation due to variation in the damping parameter μ while being invariant to the shape of the manifold. As conditions, we take different values of the damping parameter μ , which for negative values produces unstable oscillations and stabilises as μ increases above zero in a Hopf bifurcation (Fig. 1d). In addition, increasing $|\mu|$ causes continuous deformations of the limit cycle from circular to asymmetric, corresponding to slow-fast dynamics. In Fig. S6, we illustrate other examples of the application of MARBLE on this system, with different regimes of μ , and randomness in the paraboloid curvature across μ , demonstrating the difference between geometry-aware and geometry-agnostic modes of MARBLE. We repeated training five times and confirmed that the results were reproducible.

S3.2 Low-rank RNNs

We consider low-rank RNNs composed of $N = 500$ rate units in which the activation of the i -th unit is given by

$$\tau \frac{dx_i}{dt} = -x_i + \sum_{j=1}^N J_{ij} \phi(x_j) + \tilde{u}_i(t) + \eta_i(t), \quad x_i(0) = 0, \quad (\text{S20})$$

where $\tau = 100$ ms is a time constant, $\phi(x_i) = \tanh(x_i)$ is the firing rate, J_{ij} is the rank-R connectivity matrix, $u_i(t)$ is an input stimulus and $\eta_i(t)$ is a white noise process with zero mean and std 3×10^{-2} . The connectivity matrix can be expressed as

$$\mathbf{J} = \frac{1}{N} \sum_{r=1}^R \mathbf{m}_r \mathbf{n}_r^T, \quad (\text{S21})$$

for vector pairs $(\mathbf{m}_r, \mathbf{n}_r)$. For the delayed-match-to-sample task, the input is of the form

$$\tilde{u}_i(t) = w_{1i}^{\text{in}} u_1(t) + w_{2i}^{\text{in}} u_2(t), \quad (\text{S22})$$

where w_{1i}, w_{2i} are coefficients controlling the weight of inputs u_1, u_2 into node i . Finally, the network firing rates are read out to the output as

$$o(t) = \sum_{i=0}^N w_i^{\text{out}} \phi(x_i). \quad (\text{S23})$$

To train the networks, we followed the procedure in⁴⁶. The experiments consisted of 5 epochs; a fixation period of length between 100 – 500 ms chosen uniformly at random, a 500 ms stimulation period, a delay period of length between 500 – 3000 ms, a 500 ms stimulation period and a 1000 ms decision period. During training, the networks were subjected to the two inputs, whose value varied discontinuously between zero and a non-zero gain during stimulation. The networks were trained against a loss function

$$\mathcal{L} = |o(T) - \hat{o}(T)|, \quad (\text{S24})$$

where T is the length of the trial and $\hat{o}(T) = 1$ when both stimuli were present and -1 otherwise. Coefficient vectors were initially drawn from zero-mean and unit std Gaussian distributions and then optimised. For training, we used the ADAM optimiser⁶³ with moment decay rates 0.9 – 0.999 and learning rates $10^{-3} - 10^{-2}$. We trained MARBLE in geometry-agnostic mode. See Table 1 for the parameters. We repeated training five times and confirmed that the results were reproducible.

S3.3 Macaque hand reaching data

We used publically available²⁷ electrophysiology data during a centre-out instructed-delay reaching task. The neural activity was recorded using linear multielectrode arrays (V-Probe, 24-channel linear probes) from rhesus macaque motor (M1) and dorsal premotor (PMd) cortices. See²⁷ for further details on experimental procedures. Each trial began with the monkey’s hand at the centre position, after which one (or more) radial targets at 10cm from the centre position were marked visually (target onset). After a variable delay period, one of the radial targets was highlighted, indicating the go-cue for reaching. We analysed the 700ms period after the go-cue consisting of a delay followed by the reach. A total of 44 consecutive experimental sessions with a variable number of trials were considered.

For each of the 24 channels of each trial, we extracted the spike trains using the neo package in Python (<http://neuralensemble.org/neo/>) and converted them into instantaneous rates using Gaussian kernel convolution with a standard deviation of 100ms. We then binned the rates at 20ms intervals using the elephant Python package⁶⁴ to match the sampling frequency in the decoded kinematics in²⁷. Finally, we fitted a PCA across all trials in a single session to reduce the dimension of the 24-channel rates to five principal components. We trained MARBLE in geometry-aware mode (without inner product features) separately on each session, treating each of the seven movement conditions as individual manifolds. See Table 1 for parameters. We repeated training five times and confirmed that the results were reproducible.

For benchmarking, we took the trained LFADS models directly from the authors. To train CEBRA, we used the seven reach directions as labels and trained CEBRA supervised until convergence. We obtained the best results with an initial learning rate of 0.01, Euclidean norm as metric, number of iterations 10,000 and fixed temperature 1.

We followed the same procedure as in²⁷ to decode the hand kinematics from the neural trajectories. Specifically, we used Optimal Linear Estimation (OLE) to decode the x and y reaching coordinates and velocities from the neural embeddings. For each session, using 10-fold cross-validation, we fitted an OLE to map from the MARBLE embeddings to the kinematics. To assess the accuracy of decoded movements, we computed the goodness of fit (R^2) between the decoded and real velocities for both x and y before taking the mean across them. We also trained a support vector machine classifier (regularisation of 1.0 with a radial basis function) on the real kinematic movements against the known condition labels. We then evaluated the classifier on the decoded kinematics and reported the accuracy for each session.

S3.4 Rat linear maze task

We used publically available⁵⁰ electrophysiology data during a 1.6m linear track traversal both ‘leftwards’ and ‘rightwards’. The neural activity was recorded with two 8- or 6-shank silicon probes in well-isolated CA1 pyramidal single units in the hippocampus across four rats. See⁵⁰ for further details on experimental procedures. Each rat had a single recording involving multiple ‘leftward’ and ‘rightward’ movements along the linear maze. Each recording had a variable number of measured neurons, ranging from 48 neurons to 120 neurons.

For each of the animals, we extracted the spike trains using the neo package in Python (<http://neuralensemble.org/neo/>) and converted them into instantaneous rates using Gaussian kernel convolution with a standard deviation of 10ms. We then fitted a PCA across all data for a given animal to reduce the variable dimension size to 10 principle components. We trained MARBLE in geometry-aware mode (without inner product features) separately on each animal, including the original position. See Table 1 for parameters.

For benchmarking, we took the CEBRA models unchanged from the publicly available notebooks in the online documentation associated with their manuscript. For decoding position, we used a 32-dim output and 10000 iterations as per their demo notebook (https://cebra.ai/docs/demo_notebooks/Demo_decoding.html), whilst for consistency between animals we used a 3-dim output and 15000 iterations also in line with their demo notebook (https://cebra.ai/docs/demo_notebooks/Demo_consistency.html). The same output dimensions were used for MARBLE on each task, respectively.

We followed the procedure to decode the rat position along the linear maze from the neural trajectories as in the CEBRA [31]. Specifically, we fit a KNN Decoder with 36 neighbours and a

cosine distance metric using the neural embedding to predict the x position along the track. The data was split such that the initial 80% of the data was used for training, and the remaining 20% was used for testing. To assess the accuracy of decoding, we computed the mean absolute error between the predicted and true rat positions at each time point.

To assess the consistency of the embeddings across animals, we used the inbuilt functions from CEBRA for fair comparison. The embeddings are first aligned optimally using Procrustes analysis. Secondly, a linear model is fitted using the aligned embeddings of any two animals: one animal as the source (independent variables) and another as the target (dependent variables). The R^2 from the fitted model describes the amount of variance in the embedding of one animal that can be explained by another animal, i.e., a measure of consistency between their embeddings.

Table 1: Parameters used for MARBLE embedding in the different experiments

Parameters	Dataset			
	van der Pol	RNN	Macaque	Rat
Inner product features	True	False/True	False	False
k	20	15	30	15
Diffusion	False	False	True	False
Feature order, p	2	2	2	1
MLP hidden channels	32	32	100	64
MLP output channels	5	3	3/20	3/32
Number of parameters	731	2886/1339	15803	7940/9825

S4 Supplementary figures

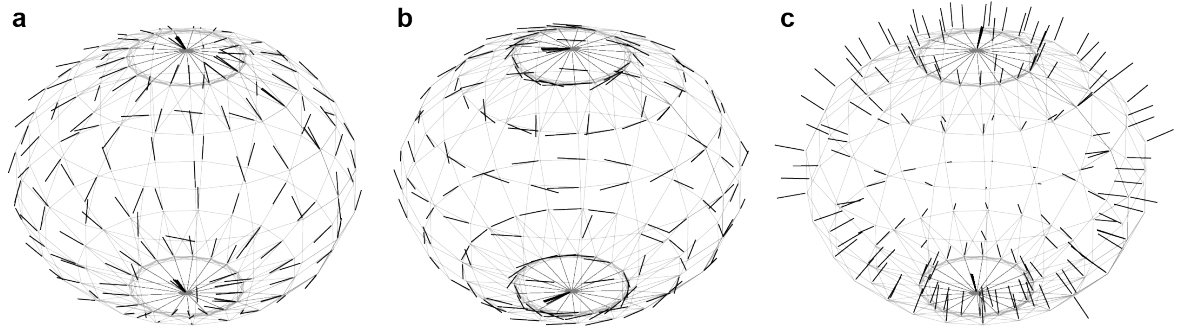


Figure S1: **Illustration of local coordinate frames.** **a,b** Local coordinate frames were fitted to eight neighbours at each point on the rectangular grid over a sphere (manifold of dimension two) embedded into \mathbb{R}^3 . Unit vectors representing within-manifold basis. **c** Unit vector represents normal to the manifold. Note that the orientation of the normal vectors is not necessarily consistent.

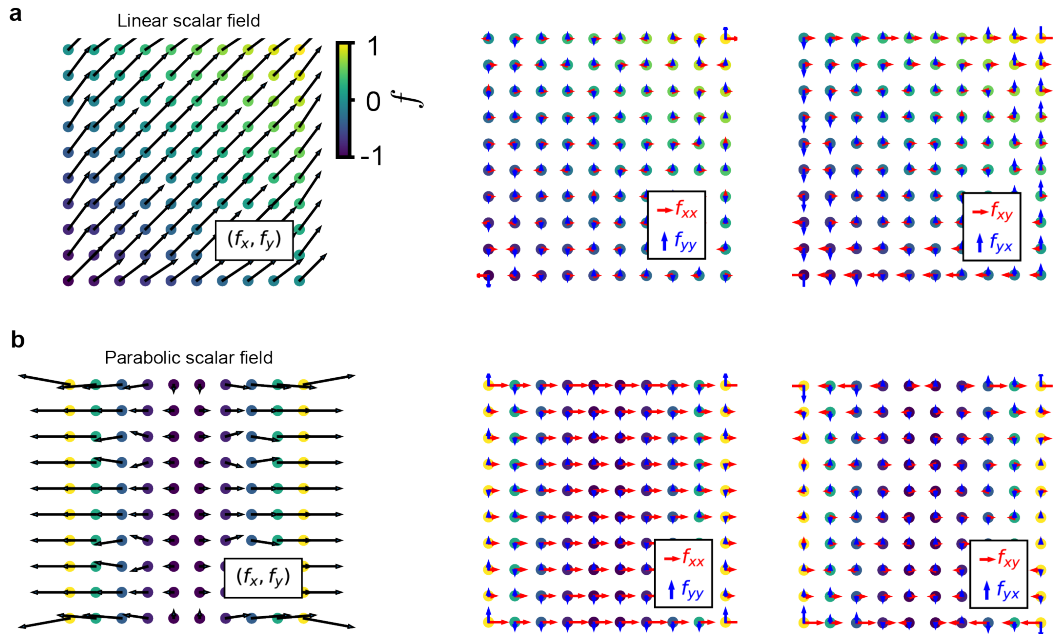


Figure S2: **Output of gradient filters.** **a** Scalar valued linear function. **b** Scalar valued parabolic function. The first column shows the output of the scalar signal convolved with the gradient filter with respect to a principal spatial coordinate, representing the directional (partial) derivatives along this direction. The second and third columns show second-order mixed partial derivatives obtained by a second application of the gradient filter to the derivative signal. In each case, we used a uniform rectangular grid with eight neighbours.

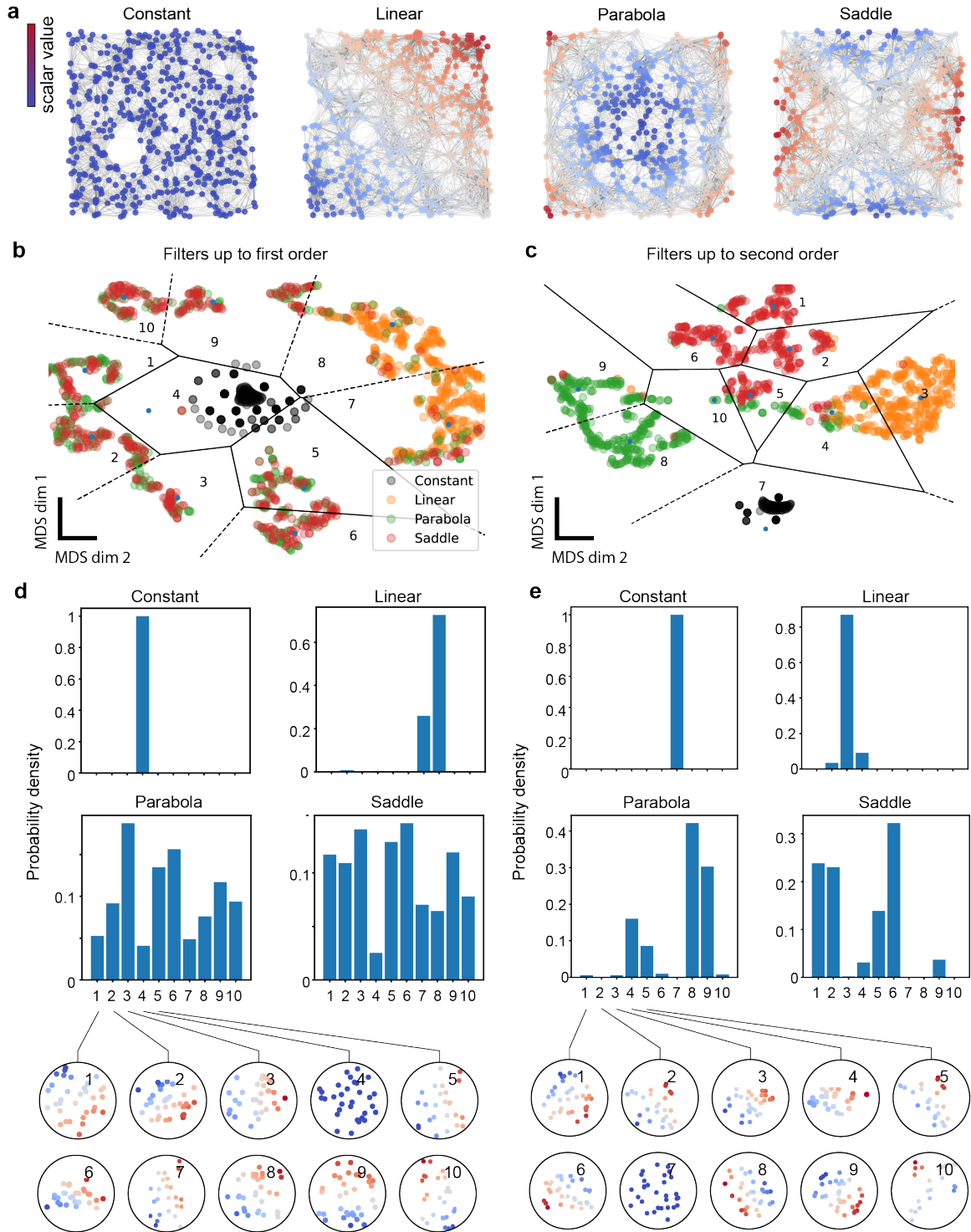


Figure S3: **Effect of filter order.** **a** Scalar functions sampled ($n = 512$) uniformly at random and fitted with a continuous k -nearest neighbour graph ($k = 15$). From left to right: constant, linear, parabola, saddle. **b** Joint embedding of local scalar fields from all functions based on first-order (1-hop) directional derivative filters. Dots represent nodes drawn from **a** with nodes close together, signifying similar signal distributions in their neighbourhoods. Black lines show the convex polygon obtained from k -means clustering (10 clusters). **c** As in **b**, but with first (1-hop) and second-order (2-hop) filters. Including second-order filters increases the clustering of features. **d** Histogram representation of the clustered neighbourhood types. The latter is shown at the bottom in circular insets. **e** As in **d** but with first and second-order filters. Second-order features better discriminate the parabola and saddle but show little difference for constant and linear fields.

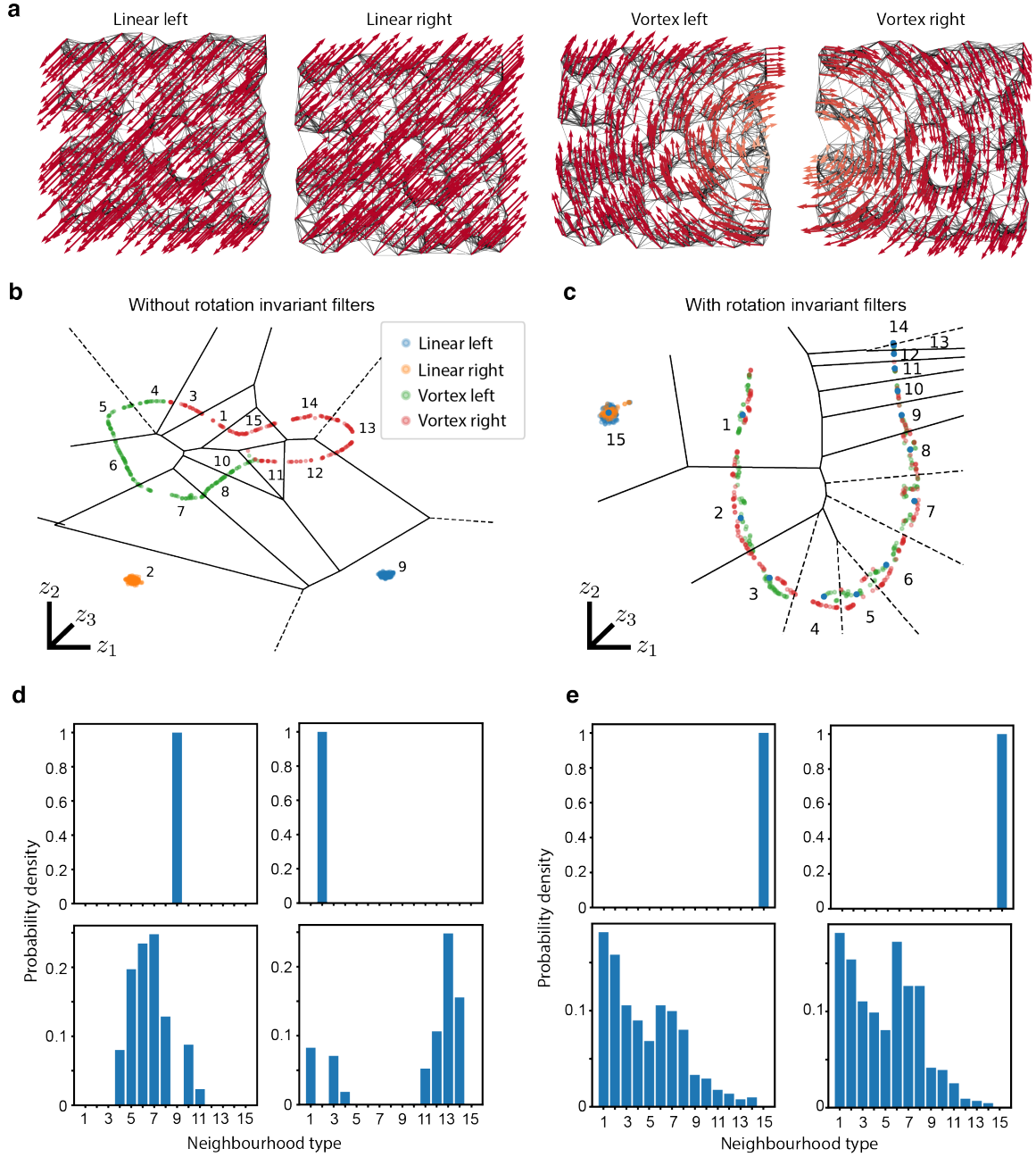


Figure S4: **Effect of rotational invariant filters.** **a** Vector fields sampled ($n = 512$) uniformly at random in the interval $[-1, 1]^2$ and fitted with a continuous k -nearest neighbour graph. **b** Joint embedding of local vector fields based on first-order (1-hop) directional derivative filters. Dots represent nodes drawn from **a** with nodes close together signifying similar signal distributions in their neighbourhoods. Features from the linear vector fields cluster together (clusters 2 and 9) while those drawn from the vortex fields fall on separate halves of a one-dimensional circular manifold corresponding to the one-parameter (angle) variation between them. **c** Same as **b** but with rotation invariant features. Features from linear fields can no longer be distinguished (cluster 15) because the filter does not learn the orientation. Features from vortex fields fall on a linear one-dimensional manifold parametrised by the distance from the centre. **d** The distribution of orientation-preserving derivative features can distinguish all fields. **e** The distribution of rotation-invariant features can discriminate linear fields from vortex fields but not the orientation.

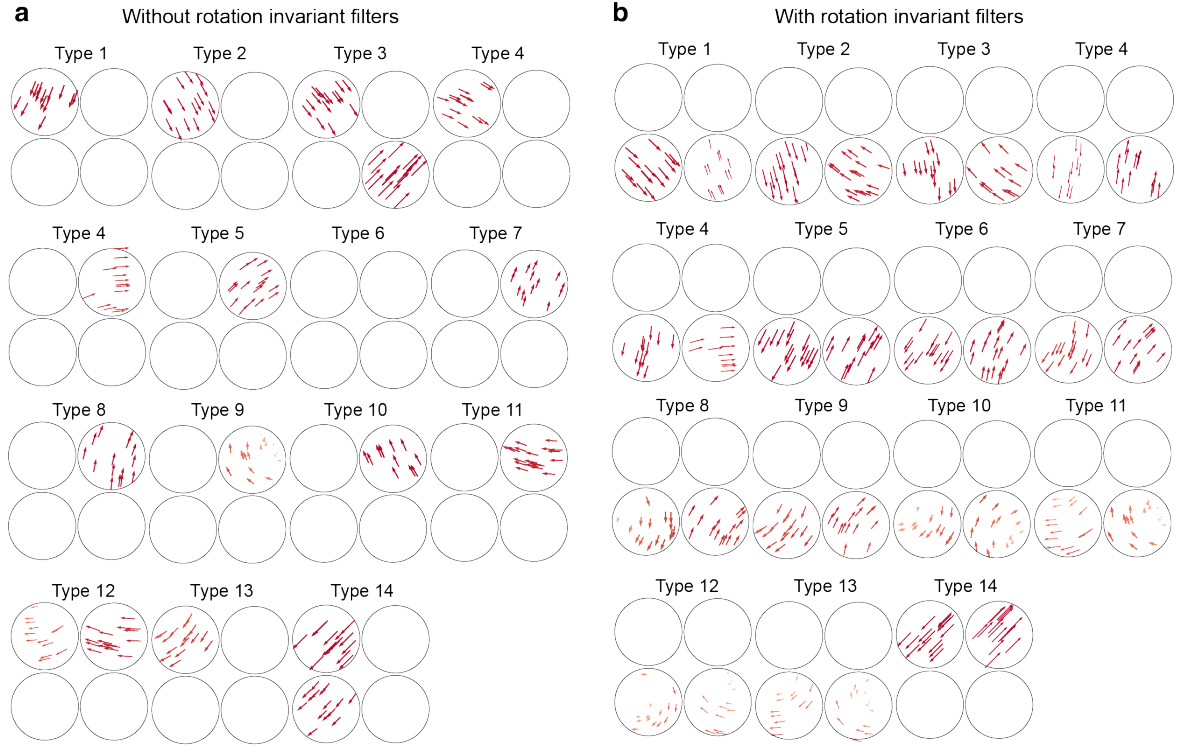


Figure S5: **Effect of rotational invariant filters on local vector field types.** Types are local vector field types with circular insets representing a local vector field drawn from each of the four fields in Fig S4. Top left: linear left; top right: linear right; bottom left vortex left; bottom right; vortex right. White insets indicate that the given type is not present in the vector field. **a** Without using rotation invariant filters the network tends to classify local vector fields into separate types. **b** With rotation invariant filters, local vector fields cluster more irrespective of the orientation. The separate types are instead distinguished more based on the expansion, and rotation properties of the features.

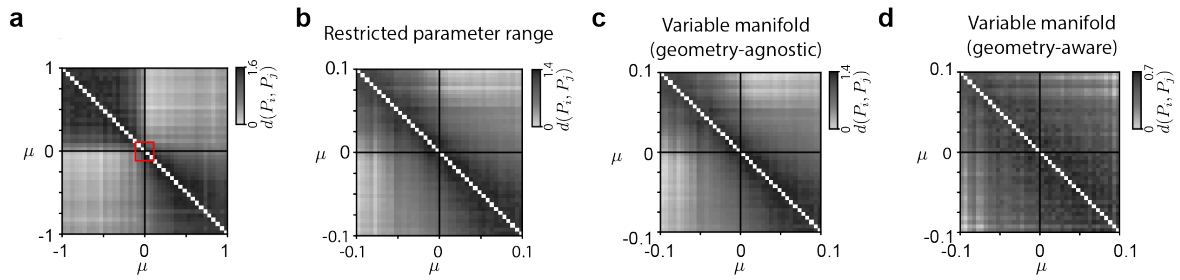


Figure S6: **Additional Van der Pol examples** We illustrate the MARBLE embedding of the Van der Pol example with 40 values of μ in the following cases. **a** Using a larger parameter range $\mu \in [-1, 1]$ increases the definition of the clusters. **b** Using a smaller parameter range $\mu \in [-0.1, 0.1]$, corresponding to the red square in a shows lower definition. **c** In geometry-agnostic mode, varying the curvature of the paraboloid $\beta(x^2 + y^2)$ by drawing β uniformly at random from $[-0.2, 0.2]$ (-0.2 to 0.2) does not alter the MARBLE embedding. **d** In geometry-aware mode, the same variation as in c destroys the cluster structure.

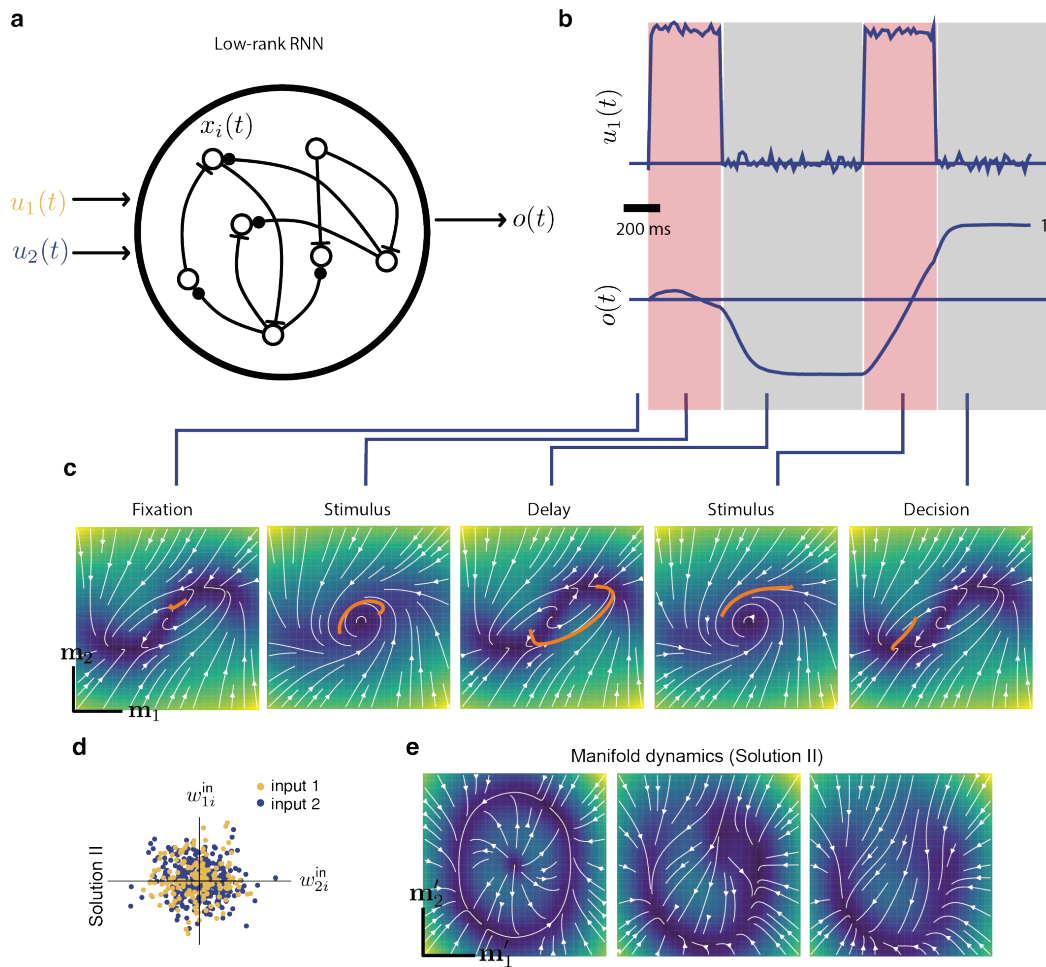


Figure S7: **Neural activities in a rank-2 RNN during the delayed-match-to-sample task.** **a** Schematic of a low-rank RNN, taking as input two stimuli and producing a decision variable as the output. Arrow endings represent inhibitory and excitatory connections. **b** Two example input patterns for one of the stimuli, and corresponding output patterns. Red and grey-shaded bands show stimulated and unstimulated periods. **c** Mean-field dynamics (heatmap and stream plot) superimposed with a sampled trajectory (orange) during one trial.

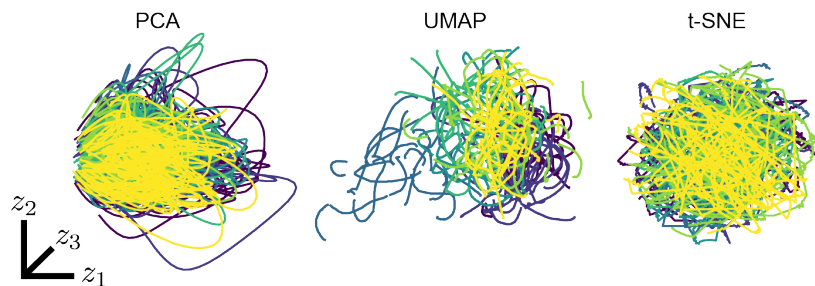


Figure S8: **Latent representations obtained using point-wise methods on the macaque reaching task, such as PCA, t-SNE and UMAP.** These methods are unsuitable to reveal the geometric structure of latent dynamics.

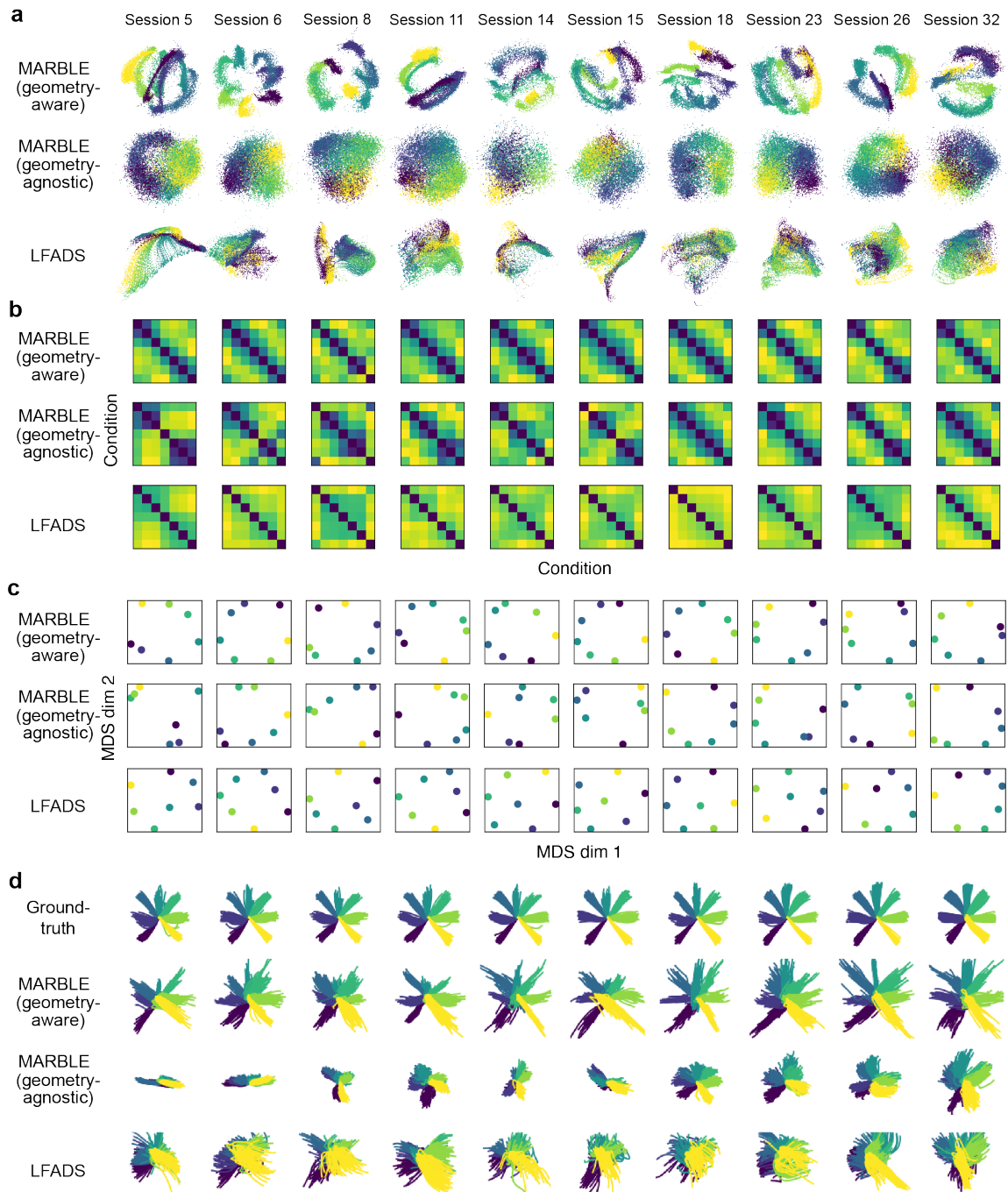


Figure S9: **Comparison of MARBLE and LFADS for learning neural dynamics for individual sessions of macaque reaching task.** **a** Feature embeddings obtained from MARBLE for various example sessions. The 3D-embedded points better reflect the arrangement of reaches in physical space when compared to LFADS. **b** The matrix of distribution distances between pairwise conditions for separate sessions shows a stronger periodic structure compared to LFADS. **c** MDS embedding of the distance matrix consistently recovers the spatial arrangement of reaches across sessions, when compared to LFADS. **d** Hand trajectories linearly decoded from MARBLE embeddings showed much stronger spatial correspondence to ground-truth kinematics than LFADS.